



HAL
open science

New measurements of cumulative photofission yields of ^{239}Pu , ^{235}U and ^{238}U with a 17.5 MeV Bremsstrahlung photon beam and progress toward actinide differentiation

M. Delarue, E. Simon, B Pérot, P.-G. Allinei, N. Estre, D. Eck, E. Payan, I. Espagnon, J. Collot

► To cite this version:

M. Delarue, E. Simon, B Pérot, P.-G. Allinei, N. Estre, et al.. New measurements of cumulative photofission yields of ^{239}Pu , ^{235}U and ^{238}U with a 17.5 MeV Bremsstrahlung photon beam and progress toward actinide differentiation. Nuclear Instruments and Methods in Physics Research Section A: Accelerators, Spectrometers, Detectors and Associated Equipment, 2022, 1040, pp.167259. 10.1016/j.nima.2022.167259 . hal-03747989

HAL Id: hal-03747989

<https://hal.science/hal-03747989>

Submitted on 9 Aug 2022

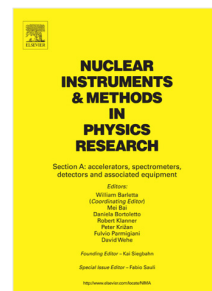
HAL is a multi-disciplinary open access archive for the deposit and dissemination of scientific research documents, whether they are published or not. The documents may come from teaching and research institutions in France or abroad, or from public or private research centers.

L'archive ouverte pluridisciplinaire **HAL**, est destinée au dépôt et à la diffusion de documents scientifiques de niveau recherche, publiés ou non, émanant des établissements d'enseignement et de recherche français ou étrangers, des laboratoires publics ou privés.

Journal Pre-proof

New measurements of cumulative photofission yields of ^{239}Pu , ^{235}U and ^{238}U with a 17.5 MeV Bremsstrahlung photon beam and progress toward actinide differentiation

M. Delarue, E. Simon, B. Pérot, P.-G. Allineï, N. Estre, D. Eck,
E. Payan, I. Espagnon, J. Collot



PII: S0168-9002(22)00600-3
DOI: <https://doi.org/10.1016/j.nima.2022.167259>
Reference: NIMA 167259

To appear in: *Nuclear Inst. and Methods in Physics Research, A*

Received date : 2 February 2022
Revised date : 31 May 2022
Accepted date : 29 June 2022

Please cite this article as: M. Delarue, E. Simon, B. Pérot et al., New measurements of cumulative photofission yields of ^{239}Pu , ^{235}U and ^{238}U with a 17.5 MeV Bremsstrahlung photon beam and progress toward actinide differentiation, *Nuclear Inst. and Methods in Physics Research, A* (2022), doi: <https://doi.org/10.1016/j.nima.2022.167259>.

This is a PDF file of an article that has undergone enhancements after acceptance, such as the addition of a cover page and metadata, and formatting for readability, but it is not yet the definitive version of record. This version will undergo additional copyediting, typesetting and review before it is published in its final form, but we are providing this version to give early visibility of the article. Please note that, during the production process, errors may be discovered which could affect the content, and all legal disclaimers that apply to the journal pertain.

© 2022 Published by Elsevier B.V.

24 zirconium. The contribution of neutron fission in the different samples has also been
25 estimated by MCNP simulations in order to assess as precisely as possible the photofission
26 yields. Finally, 26 cumulative photofission product yields are reported for ^{239}Pu , 28 for
27 ^{238}U and 26 for ^{235}U , with half-lives ranging from 14 min to more than 3 days, some of
28 them being not recorded so far in the literature. Among these reported photofission product
29 yields, 18 have been measured for all 3 actinides, which can thus be used for their
30 discrimination. A differentiation criterion based on delayed gamma-ray ratios has been
31 established to determine the most efficient photofission product couples to estimate the
32 enrichment of a $^{235}\text{U}/^{238}\text{U}$ mixture or the fissile fraction ($^{235}\text{U}+^{239}\text{Pu}$)/actinide mass in a
33 mixture of uranium and plutonium.

34 1. Introduction

35 The safety related to the management of radioactive waste (transportation, interim storages
36 and final repositories) is ensured with an accurate non-destructive characterization of their
37 actinide content in relation with the corresponding specifications. Among active non-
38 destructive methods that have been studied to address this characterization in the case of
39 large and dense packages, such as concrete drums [1]-[5], Active Photon Interrogation
40 based on the photofission phenomenon, is the only one that can bring a sufficient signal
41 from the nuclear materials inside the package. Specifically, the detection of delayed gamma
42 radiation emitted by fission products induced by high-energy photons has the potential to
43 assess the actinide mass present in a package, and possibly to distinguish fissile nuclei (that
44 can undergo thermal neutron fission, e.g. ^{235}U and ^{239}Pu) and fertile nuclei (that can absorb
45 a neutron, leading to the formation of a fissile nuclei, e.g. ^{238}U). To that extent, photofission
46 yields of the actinides of interest must be known precisely. Even though nuclear data
47 related to photofission yields of ^{238}U exist, they sometimes present significant
48 discrepancies, even in recent studies [6]-[12]. Photofission yield data are even scarcer for
49 fissile isotopes such as ^{235}U [7][12] and ^{239}Pu [11]-[14], hence the need to perform new
50 measurements.

51 The potential of analyzing the delayed gamma ray signal following fission to obtain an
52 actinide identification information has already been demonstrated in the past. Hollas *et al.*

53 [15] and Beddingfield *et al.* [16] have reported the use of delayed gamma-ray ratios for
54 actinide differentiation, respectively for photofission and thermal neutron fission. Further
55 experimental work conducted by Gmar *et al.* [17] pointed out variations of the delayed
56 gamma-ray emissions for uranium samples of different enrichments. Also, Carrel *et al.* [1]
57 brought information about the delayed gamma emission following photofission in mixed
58 samples of ^{235}U and ^{238}U . Besides, the uranium isotopes differentiation in an 870 L waste
59 drum by using delayed gamma-ray ratios has already been investigated experimentally with
60 a mockup package [1] and by using Monte-Carlo simulations in the work of Simon *et al.*
61 [5]. Furthermore, photofission products emitting several gamma rays can be used as
62 attenuation indicators to estimate the depth at which nuclear materials are localized inside
63 the package [18].

64 In the frame of a long-term research program conducted by the Nuclear Measurement
65 Laboratory of CEA IRESNE Institute in France, this work follows the study recently
66 reported in [19], which provided cumulative photofission yields of ^{235}U and ^{238}U with a
67 15.8 MeV Bremsstrahlung beam produced by a linear electron accelerator (LINAC) in
68 CINPHONIE casemate of CHICADE nuclear facility [20]. We present here new
69 cumulative photofission yields for ^{239}Pu , and again for ^{235}U and ^{238}U , which are measured
70 with the same setup but with an endpoint electron energy of 17.5 MeV. To this aim, the
71 characterization of the photon beam is first carried out by photon activation analysis with
72 different samples of Au, Ni, U, Zn and Zr. Then we estimate the neutron fission rates in
73 the different samples with MCNP, in view to subtract it from the total fission rate and thus
74 obtain the photofission yields. We also identify photofission products of interest for the
75 differentiation between fissile and fertile actinides.

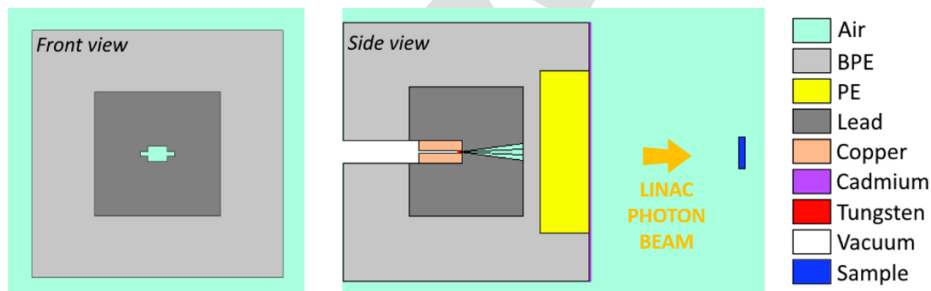
76 2. Experimental setup

77 Experiments were performed by using a Bremsstrahlung photon beam produced by a
78 Saturne LINAC located in the CINPHONIE irradiation cell at CEA Cadarache. In pulse
79 mode, the LINAC accelerates electrons up to 21 MeV. The electrons strike a 5 mm thick
80 tungsten target and a part of their kinetic energy is converted into Bremsstrahlung radiation.
81 The pulse frequency and width are 200 Hz and 4.1 μs , respectively, and the peak current is
82 100 mA at the target entrance. A 20 cm thick lead collimator allows focusing the beam on

83 the actinide samples, surrounded by a 20 cm thick shield made of borated polyethylene
 84 (BPE) and polyethylene to limit the photoneutron flux reaching the samples, and thus to
 85 minimize neutron fissions. A cadmium (Cd) layer of 2 mm was added on the front face to
 86 complete the thermal neutron absorption occurring in BPE. A picture of the LINAC
 87 configuration and the corresponding simulated model with a materials description are
 88 respectively given in Figure 1 and Figure 2. During the experiments, the photon dose rate
 89 at 1 m from the tungsten target measured by an ionization chamber was 33 Gy/min.



90
91 *Figure 1: Saturne LINAC with collimator and neutron shielding.*



92
93 *Figure 2: MCNP model of the irradiation configuration (LINAC, lead collimator, neutron shielding and sample).*

94 The photon flux at the output of the collimator aperture being not known precisely,
 95 nor the endpoint-energy of the Bremsstrahlung spectrum expected around 16 MeV, a
 96 characterization of the photon beam produced by the LINAC is performed using photon
 97 activation of reference materials, following the method described in our previous work
 98 [19]. The main steps and results of the beam characterization are described in section 3.
 99 The pellets irradiated to this aim and positioned in the axis of the LINAC photon beam are
 100 described in Table 1. The other pellets in Figure 3 are made of indium (left) and magnesium
 101 (right). They were originally designed to be used as neutron activation spectrometers [21]
 102 and were irradiated to estimate the photoneutron production in the CINPHONIE irradiation
 103 cell (not reported in this paper but used qualitatively in section 4).

104

Element	Mass (g)	Diameter (mm)	Thickness (mm)	Position on Figure 3
Au	0.045	5	0.05	1
Zn	2.70	19	1.33	2
Ni	10.03	22	3	3

Table 1: Characteristics of the metal pellets irradiated for the photon beam characterization.

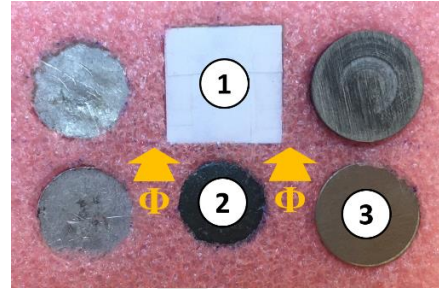


Figure 3: Position of the pellets on their support in view of their common irradiation.

107 Three actinide samples were irradiated: a sample of Depleted Uranium (DU) which is
 108 the same as we used in our previous work [19], a sample of Highly Enriched Uranium
 109 (HEU) and a sample of plutonium (Pu). The different samples are described in Table 2.

110

Table 2: Description of the actinide samples.

	Uranium		Plutonium	
	DU	HEU	Sample	Pu
Mass	> 100 g and < 1 kg	> 1 g and < 100 g	Mass	~1 g
²³⁵ U content	0.3 %	> 90 %	Isotopic composition	²³⁹ Pu: 83 % ²⁴⁰ Pu: 12 %
Composition	Metallic uranium	Metallic uranium core held between Zircaloy sheets	Chemical form	PuO ₂ powder mixed with resin
Dimension	1 cm thickness	< 1 mm thickness	Density	1.98 g.cm ⁻³
Density	18.96 g.cm ⁻³	Fissile core: 18.96 g.cm ⁻³ Zircaloy: 6.56 g.cm ⁻³		

111

112 Since the DU sample is 1 cm thick and composed of metallic uranium of density
 113 18.96 g.cm⁻³, significant self-attenuation effects occur both for the interrogating photon
 114 flux and the delayed gamma rays emitted by photofission products. Therefore, correction
 115 factors are applied in order to calculate the photofission product yields (see section 4.2).
 116 The plutonium sample is composed of 83 % of ²³⁹Pu and 12 % of ²⁴⁰Pu. In this work, we
 117 will consider that the sample is made of 95 % of ²³⁹Pu since the photofission cross sections
 118 for these two isotopes are similar, as seen in Figure 4. It can also be noted that the calculated
 119 photofission rates are the same with the real isotopic composition of the plutonium sample
 120 and with 100 % of ²³⁹Pu. Based on the work of Bernard *et al.* [22] with the GEF code, we
 121 can also assume that the cumulative photofission yields of ²³⁹Pu and ²⁴⁰Pu are very close,
 122 enabling us to consider our plutonium sample as a ²³⁹Pu sample without introducing a
 123 significant bias in our analyses.

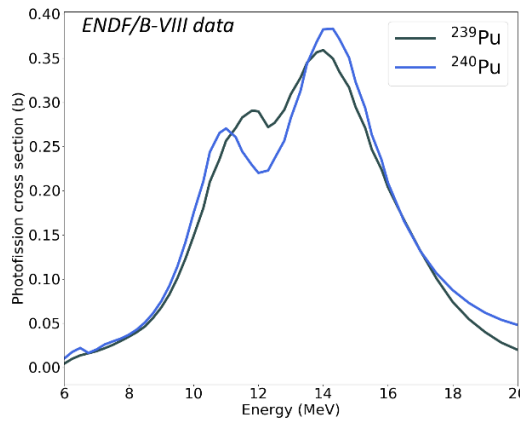


Figure 4: Photofission cross sections of ^{239}Pu and ^{240}Pu [23].

124

125

126 For each actinide sample, a 2 h irradiation with the LINAC is followed by an automatic
 127 transfer from the irradiation to the counting position, lasting less than a minute and noted
 128 “cooling time” in further activation analysis equations. The samples used to characterize
 129 the Bremsstrahlung photon beam were irradiated all together, on the support shown in
 130 Figure 3, and transferred to a low-background spectrometer located in another
 131 experimental room. Table 3 summarizes the distance and time parameters related to each
 132 sample.

133

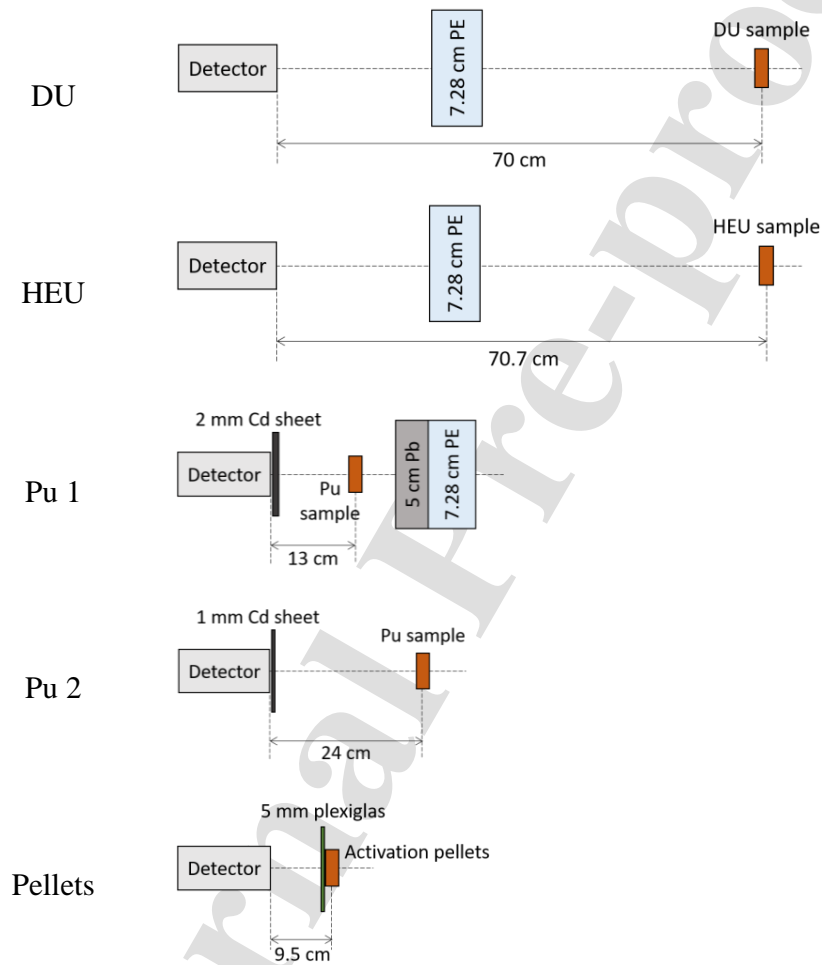
Table 3: Experimental distances and timings.

Sample	Denomination	Target-sample distance (cm)	Sample-detector distance (cm)	Irradiation time	Cooling time*	Counting time
Depleted Uranium	DU	102.0	70.0	2 h	19 min	42 h
Highly Enriched Uranium	HEU	102.7	70.7	2 h	42 s	24 h
Plutonium	Pu 1	45.4	13.0	2 h	50 min	24 h
	Pu 2	113.8	24.0	2 h	10 min	21 h
Activation samples (Au, Ni, Zn)	Pellets	88.0	9.5	1 h	390 s	145 h

134 *See text for the reason of the different cooling times

135 Figure 5 shows the layout for every detection configuration. Different screens were added
 136 depending on the irradiated samples. For the DU and HEU measurements, only a
 137 polyethylene screen was inserted in front of the detector to protect the crystal from fast
 138 photoneutron damage during irradiation (it also allows reducing the count rate). A thin
 139 cadmium sheet was added in front of the detector to cut the passive emission component
 140 of the plutonium sample (59.5 keV due to ^{241}Am). For the “Pu 1” measurement, a lead

141 shield and a polyethylene screen were used to diminish neutron activation of the detector
 142 during irradiation and to reduce the dead-time related to the activation of the surroundings
 143 during the measurement (the plutonium sample is inserted between the detector and these
 144 shields by a mechanical device). Concerning the metal pellets measurement for the photon
 145 beam characterization, the 5 mm Plexiglas screen corresponds to the sample holder.



146 *Figure 5: Experimental configuration layout for detection.*

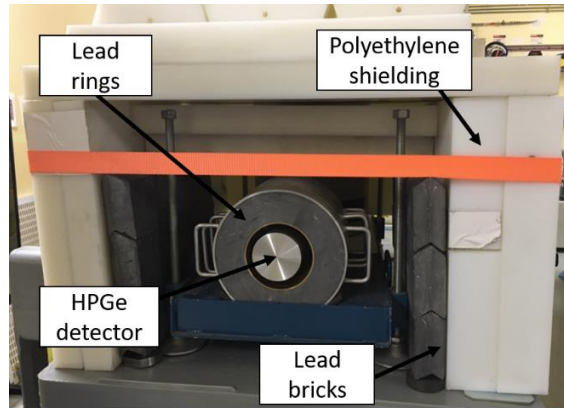
147 The gamma rays of fission and activation products are measured with a 50 % relative
 148 efficiency n-type coaxial high-purity germanium detector (HPGe, ORTEC GMX50-83-1-
 149 PL) equipped with a transistor-reset preamplifier and coupled to a LYNX Digital Signal
 150 Analyzer (CANBERRA) driven by Genie2000 software (MIRION Technologies). The rise
 151 time and flat top parameters are respectively set at 2 μ s and 0.5 μ s following an
 152 optimization. The energy resolution is 2.0 keV (FWHM) at the 1332.5 keV gamma line of

153 ^{60}Co . Although an n-type HPGe crystal is used to limit neutron damage, the detector is
154 shielded by lead and polyethylene, as shown in Figure 6. The analysis of actinide delayed
155 gamma spectra is performed with the MAGIX software developed by CEA LIST, in
156 collaboration with CEA IRESNE Nuclear Measurement Laboratory, to analyze complex
157 gamma- and X-ray spectra measured with HPGe detectors. This automatic software, based
158 on CEA LIST know-how in complex spectrum processing [24][25], performs a complete
159 analysis including energy calibration, identification of radionuclides, peak deconvolution,
160 determination of a relative detection efficiency as a function of energy, activity calculation
161 for each radionuclide if the absolute efficiency is provided by the end-user, and otherwise
162 activity ratios using the relative efficiency. One of its main features is to include iterative
163 steps to identify the radionuclides likely to be associated with each peak of the spectrum,
164 based on the gamma- and X-rays given in JEFF-3.3 database [26] and on a list of possible
165 radionuclides provided by the user.

166 In order to monitor and correct for the varying dead time during the counting period
167 (due to the rapidly decreasing total count rate), the delayed photofission gamma spectra of
168 the actinide samples were acquired sequentially every 60 s with a spectrum reset. The dead
169 time compensation is a live-time correction, which was assessed to be reliable for dead
170 times below 50 % with the two-source method ($^{88}\text{Y} + ^{137}\text{Cs}$ as the reference, and ^{152}Eu as
171 the perturbing source responsible of an increasing count rate), prior to LINAC acquisitions.
172 The initial dead times after irradiation were 80 % and 39 %, respectively, for DU and HEU
173 uranium samples. Therefore, the DU sample spectrum was analyzed only after a 19 min
174 cooling time, hence the impossibility to measure short half-life photofission products. As
175 the first measurement of the plutonium sample (Pu 1, cf. Table 3) had an initial dead time
176 of 94 % (dead time fell below 50 % only after 50 min), another irradiation further from the
177 LINAC tungsten target was performed (Pu 2, cf. Table 3), leading to an initial dead time
178 of 61 % that fell below 50 % after 10 min of cooling.

179 The **non-actinide** activated metallic samples used for the beam characterization were
180 transferred inside a low-background spectrometer with a 9 % relative efficiency HPGe
181 detector (CANBERRA BEGe 2020) in a lead shield, with inner walls covered by a copper
182 layer to cut lead X-rays. The detector is connected to a digital spectrometer (CANBERRA
183 DSP9660) and the resolution is 1.75 keV (FWHM) at the 1332.5 keV gamma line of ^{60}Co .

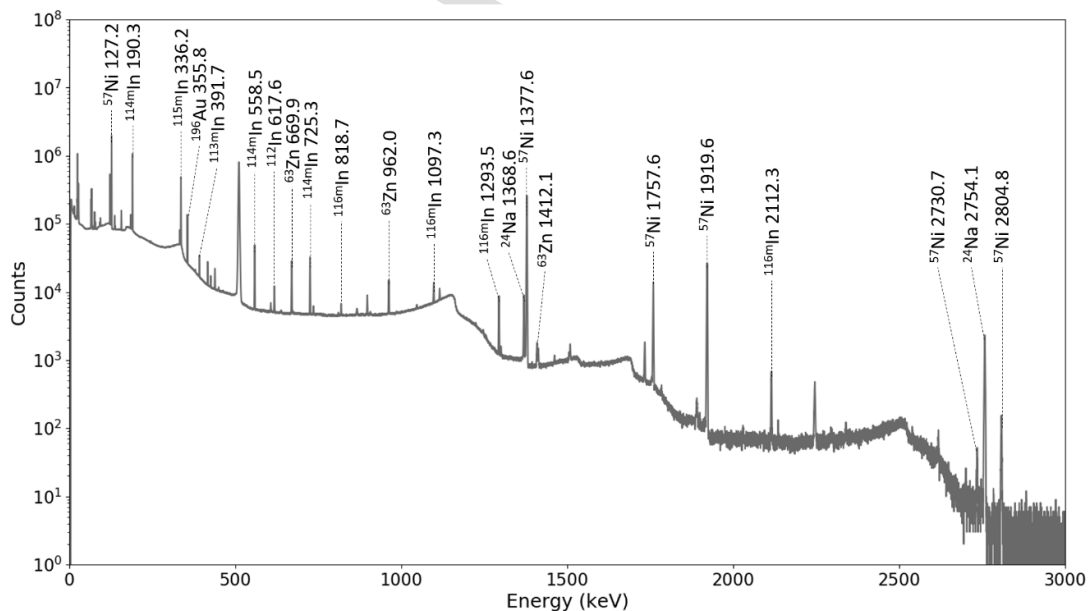
184 The gamma spectrum from the activation pellets was recorded during 6 days after
 185 irradiation. Regular resets of the spectrum acquisition were also undertaken to properly
 186 correct for dead time. These gamma spectra were analyzed with Genie2000 software
 187 (MIRION Technologies).



188
 189 *Figure 6: Shielded germanium detector.*

190 3. LINAC photon beam characterization

191 The photon and neutron activation spectrum of the thin metallic pellets irradiated to
 192 characterize the photon beam of the LINAC is given in Figure 7.



193
 194 *Figure 7: Activation gamma spectrum of the metallic pellets shown in Figure 3.*

195 The detected gamma rays due to (γ,n) activation reactions of gold, zinc and nickel isotopes
 196 are reported in Table 4, as well as those of ^{238}U activation in the DU sample and ^{90}Zr
 197 activation in the HEU sample (Zircaloy frame, see Table 2). Half-lives and gamma-ray
 198 energies are taken from JEFF-3.3 nuclear database [26]. The net areas of the gamma-ray
 199 peaks are from the spectra analysis with Genie2000 software. The net area statistical
 200 uncertainty is $\sigma(N_{\text{counts}}) = \sqrt{N_{\text{counts}} + 2B}$, where B is the Compton background under
 201 the total absorption peak.

202 *Table 4: Activation gamma rays due to the (γ,n) reaction analyzed to characterize the LINAC photon beam.*

Activated isotope	Activation product	Half-life	γ -ray line analyzed (keV)	Net area N_{counts}
^{197}Au	^{196}Au	6.17 days	355.8	549721 ± 741
^{58}Ni	^{57}Ni	35.9 h	1377.6	2411040 ± 1553
^{238}U	^{237}U	6.75 days	208.0	1310540 ± 1145
^{64}Zn	^{63}Zn	38.3 min	669.9	157242 ± 397
^{90}Zr	$^{89\text{m}}\text{Zr}$	250.8 s	587.8	37223 ± 193
	^{89}Zr	3.26 days	/	/
	$^{89\text{m}}\text{Y}^*$	15.7 s	909.0	22248 ± 472

203 * From the ^{89}Zr and $^{89\text{m}}\text{Zr}$ decays

204 Since the characteristics of the interrogating photon beam were not known precisely,
 205 photon activation of these materials is used to estimate the endpoint-energy of the
 206 bremsstrahlung beam and the photon flux, as described in our previous work [19]. The
 207 method is based on the differences in the photonuclear cross-sections [27], since each
 208 material has a different energy threshold and cross-section for the (γ,n) reaction. Therefore,
 209 we are looking for the incident photon flux characteristics that best matches the observed
 210 activation of five materials. To this aim, we assume a semi-Gaussian shape of the electron
 211 energy distribution, see further Figure 8, of which we are looking for the optimal endpoint-
 212 energy and width at half-maximum.

213 The endpoint-energy was varied from 15 MeV to 18.5 MeV with 0.5 MeV steps, and the
 214 width at half-maximum from 0 MeV (mono-energy distribution) to 2 MeV with 0.5 MeV
 215 steps. For each of the 40 pairs of parameters, MCNP [28] simulations were performed by
 216 impinging electrons of the considered energy distribution on the LINAC tungsten target to
 217 produce the Bremsstrahlung photon beam. Then, the number of (γ,n) reactions in each
 218 activated sample was numerically evaluated, corresponding to the convolution of the

219 resulting photon flux on the different materials with their reaction cross-sections. Finally,
 220 an experimental photon flux is calculated for each activated isotope (^{197}Au , ^{58}Ni , ^{238}U , ^{64}Zn
 221 and ^{90}Zr) by using the net area of the peaks listed in Table 4. As a result, five photon fluxes
 222 are obtained for each couple of beam parameters. The most probable electron energy
 223 distribution is then identified as the one minimizing the squared differences between these
 224 five flux values. In our case, the electron energy distribution with an endpoint-energy of
 225 17.5 MeV and a 0.5 MeV width at half-maximum provides the most consistent photon
 226 fluxes for all the materials, as reported in Table 5.

227 *Table 5: Experimental photon fluxes calculated for the five materials with the most probable electron energy*
 228 *distribution.*

Activated isotope	$\Phi_{88\text{cm},\text{exp}}$ (photons.cm ⁻² .s ⁻¹)
^{197}Au	$(6.82 \pm 0.87) \times 10^{10}$
^{58}Ni	$(7.31 \pm 0.89) \times 10^{10}$
^{238}U	$(6.07 \pm 0.75) \times 10^{10}$
^{64}Zn	$(6.57 \pm 0.84) \times 10^{10}$
^{90}Zr	$(5.97 \pm 0.75) \times 10^{10}$
Mean photon flux $\bar{\phi} = (6.55 \pm 0.94) \times 10^{10}$ photons.cm ⁻² .s ⁻¹	

229 The uncertainty on the experimental photon flux for each material is calculated as a
 230 quadratic combination of the main following sources of uncertainty:

- 231 - a relative uncertainty estimated to 10 % on the (γ,n) cross-section of the activated
 232 isotopes, according to the EXFOR cross-section library [29]. As an example, the
 233 $^{197}\text{Au}(\gamma,n)^{196}\text{Au}$ reaction cross-section uncertainty is about 10 % in the work of
 234 Plaisir *et al.* [30];
- 235 - a relative uncertainty of 7 % on the detection efficiency to take into account both
 236 the detector intrinsic efficiency (less than 5 % thanks to a fine detector model,
 237 optimized using reference measurements of standard sources) and the modeling of
 238 the experimental set-up (uncertainties on samples and on equipment dimensions,
 239 set at 5 % based on our experience of such simulations). Intrinsic and geometric
 240 efficiency uncertainties are combined in quadratic sum, leading to a 7 % relative
 241 uncertainty on detection efficiency;

- 242 - the statistical uncertainty related to MCNP simulation results, which is lower than
 243 2 % for all activation calculations;
- 244 - the uncertainties on the radioactive decay constants of the activation products and
 245 their gamma-ray intensities, provided by JEFF-3.3 database [26], which are lower
 246 than 4 %;
- 247 - the uncertainty on the net area of the gamma rays reported in Table 4, which is at
 248 most 2.1 %. It is provided by the Genie2000 software and takes into account the
 249 uncertainty related to the counting statistics as well as that related to the fitting
 250 procedure.

251 The uncertainty associated to the mean photon flux is here estimated, conservatively, as
 252 the quadratic combination of the mean uncertainty of the five calculated photon fluxes
 253 (around 12 %) and the standard deviation of the photon fluxes obtained with the five
 254 materials:

$$255 \quad \frac{\sigma_{distribution}}{\bar{\phi}} = \frac{1}{\bar{\phi}} \sqrt{\frac{(\phi_{Au}-\bar{\phi})^2 + (\phi_{Ni}-\bar{\phi})^2 + (\phi_U-\bar{\phi})^2 + (\phi_{Zn}-\bar{\phi})^2 + (\phi_{Zr}-\bar{\phi})^2}{5}} = 7 \%;$$

256

257 The electron distribution corresponding to the most likely, 17.5 MeV endpoint energy and
 258 0.5 MeV width at half maximum, is shown in Figure 8, and the corresponding
 259 Bremsstrahlung photon distribution calculated with MCNP is given in Figure 9.

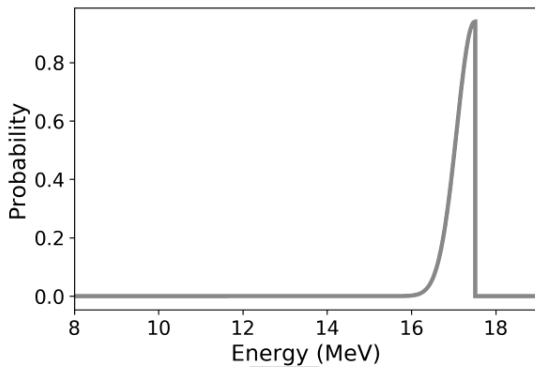


Figure 8: Most probable electron energy distribution (source of MCNP flux and reaction rate calculations).

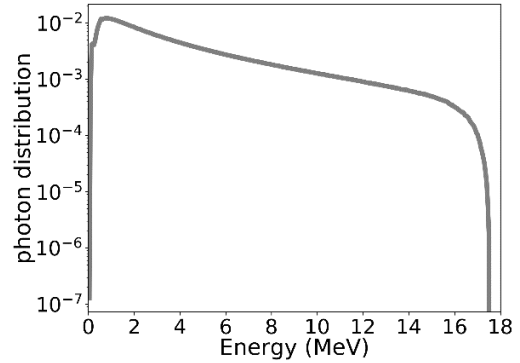


Figure 9: Bremsstrahlung photon energy distribution (normalized) calculated with MCNP and the electron energy distribution of Figure 8.

260 The mean experimental photon flux of $(6.55 \pm 0.94) \times 10^{10} \text{ photons.cm}^{-2}.\text{s}^{-1}$, at the
 261 center of the beam and 88 cm away from the tungsten target, will be used to normalize
 262 MCNP simulation results that are given per electron impinging on the tungsten target.

263 4. Comparison of simulated photofission and neutron fission rates

264 The photofission rate in the samples is defined by (1) for a mixture of n actinides.

$$\tau_p = \frac{N_A}{\mathcal{M}} \left(\sum_{i=1}^n m_i \int_{E_{threshold}}^{E_{max}} \varphi(E) \sigma_{i(\gamma,f)}(E) dE \right) \quad (1)$$

265 Where:

- 266 - τ_p is the photofission rate in s^{-1} ;
- 267 - N_A is the Avogadro constant, equals to $6.02 \times 10^{23} \text{ mol}^{-1}$;
- 268 - \mathcal{M} is the molar mass of the actinide mixture, expressed in g.mol^{-1} ;
- 269 - m_i is the mass of actinide i in the sample, in g;
- 270 - $E_{threshold}$ and E_{max} are respectively the threshold energy of the photofission
271 reactions, around 6 MeV, and the Bremsstrahlung endpoint-energy, 17.5 MeV in
272 our case;
- 273 - $\varphi(E)$ is the Bremsstrahlung photon flux at the energy E in the sample, in
274 $\text{photons.cm}^{-2}.\text{s}^{-1}$;
- 275 - $\sigma_{i(\gamma,f)}(E)$ is the photofission reaction cross-sections at the energy E for actinide i ,
276 in cm^2 .

277 The uncertainty on the photofission rate calculated with MCNP is the quadratic
278 combination of the following uncertainties:

- 279 - a 14.3 % relative uncertainty on the Bremsstrahlung photon flux, determined in
280 section 3, $(6.55 \pm 0.94) \times 10^{10} \text{ photons.cm}^{-2}.\text{s}^{-1}$ (see Table 5);
- 281 - a 0.1 % relative statistical uncertainties on MCNP calculations for the photofission
282 rate in the plutonium, DU and HEU samples;
- 283 - a 2 % uncertainty on the photofission cross-section, according to datasets available
284 in the EXFOR library [29];

285 Finally, using the characteristics of the beam (electron energy distribution and photon flux)
286 and the experimental position of the samples with respect to the tungsten target, the
287 photofission rates in the samples calculated with MCNP are:

$$288 \tau_{p,\text{Pu } 1} = (1.32 \pm 0.19) \cdot 10^7 \text{ s}^{-1}$$

$$289 \tau_{p,\text{Pu } 2} = (2.33 \pm 0.34) \cdot 10^6 \text{ s}^{-1}$$

$$\tau_{p,DU} = (2.66 \pm 0.38) \cdot 10^8 \text{ s}^{-1}$$

$$\tau_{p,HEU} = (3.38 \pm 0.48) \cdot 10^7 \text{ s}^{-1}$$

It was shown in our previous work [19] that neutron fissions in the actinides are mainly due to fast neutrons produced in the samples themselves. Indeed, the neutron shielding around the LINAC head (tungsten target and lead collimator), composed of borated polyethylene and cadmium, was proven to be efficient since the presence of thermal neutrons was not observed from neutron activation of the metallic pellets. Indeed, although radiative capture gamma rays of ^{116m}In , due to the $^{115}\text{In}(n,\gamma)^{116m}\text{In}$ activation reaction, highlight the presence of epithermal neutrons with an energy larger than 0.5 MeV (not absorbed by the cadmium foil in front of the LINAC head), thermal neutrons are not detected through the activation of the gold foil. Indeed, we do not observe in the gamma spectrum the 411.8 keV line of ^{198}Au , which was expected from the $^{197}\text{Au}(n,\gamma)^{198}\text{Au}$ reaction, despite a high cross section for thermal neutrons of 100 b ($1 \text{ b} = 10^{-28} \text{ m}^2$) at 0.025 eV according to ENDF/B-VIII.0 library [23].

MCNP simulations were conducted to characterize the origin of the fissions occurring in the samples, i.e. photofission vs. neutron fissions are reported in Table 6, in order to calculate the photofission yields as precisely as possible for the three actinides.

Table 6: Origin of the fissions in the different actinide samples.

Plutonium		Uranium		
Sample	Pu	Sample	DU	HEU
Photofissions	98.3 %	Photofissions of ^{238}U	94.2 %	3.6 %
Neutron fissions	1.7 %	Photofissions of ^{235}U	-	93.1 %
		Neutron fissions of ^{238}U	5.8 %	-
		Neutron fissions of ^{235}U	-	3.3 %

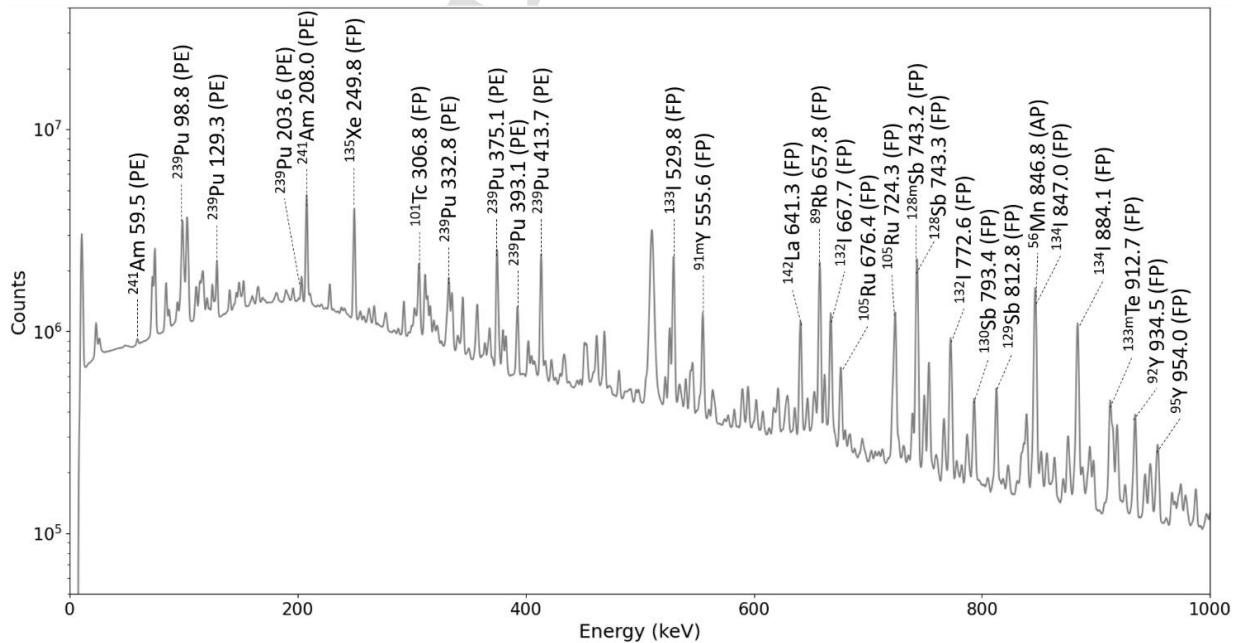
In the plutonium sample, the only 1.7 % of neutron fissions will be subtracted to obtain the photofission yields of ^{239}Pu . Besides, given the similarity between the photofission cross sections of ^{239}Pu and ^{240}Pu (cf. Figure 4), we assume that all photofissions occur on ^{239}Pu . Concerning the DU sample with a ^{235}U content of 0.3 %, we consider that all fissions occur on ^{238}U . Among them, 5.8 % are ^{238}U fissions caused by fast neutrons. As a result, the delayed gamma rays measured with the DU sample are used to directly calculate the ^{238}U

315 photofission products cumulative yields, after subtraction of the neutron fission
 316 contribution. In the HEU sample, however, 3.6 % of photofissions occur on ^{238}U and
 317 93.1 % on ^{235}U . Moreover, 3.3 % of fissions are fast neutron fissions on ^{235}U . Therefore,
 318 the ^{238}U contribution to photofission and the ^{235}U contribution to neutron fission will be
 319 subtracted to calculate the ^{235}U photofission products cumulative yields.

320 5. Cumulative yields of ^{239}Pu , ^{235}U and ^{238}U photofission products

321 Figures 10 to 12 show the delayed gamma spectrum of the plutonium sample (denoted
 322 as the Pu 1 measurement in Table 3) recorded during 24 h, after a 2 h irradiation with a
 323 17.5 MeV endpoint energy Bremsstrahlung photon beam and a 35 s cooling time. The
 324 notations used are PE for Passive Emission, AP for Activation Product and FP for Fission
 325 Product. Note that delayed gamma spectra for DU and HEU photofission products have
 326 already been presented in our previous work [19].

327

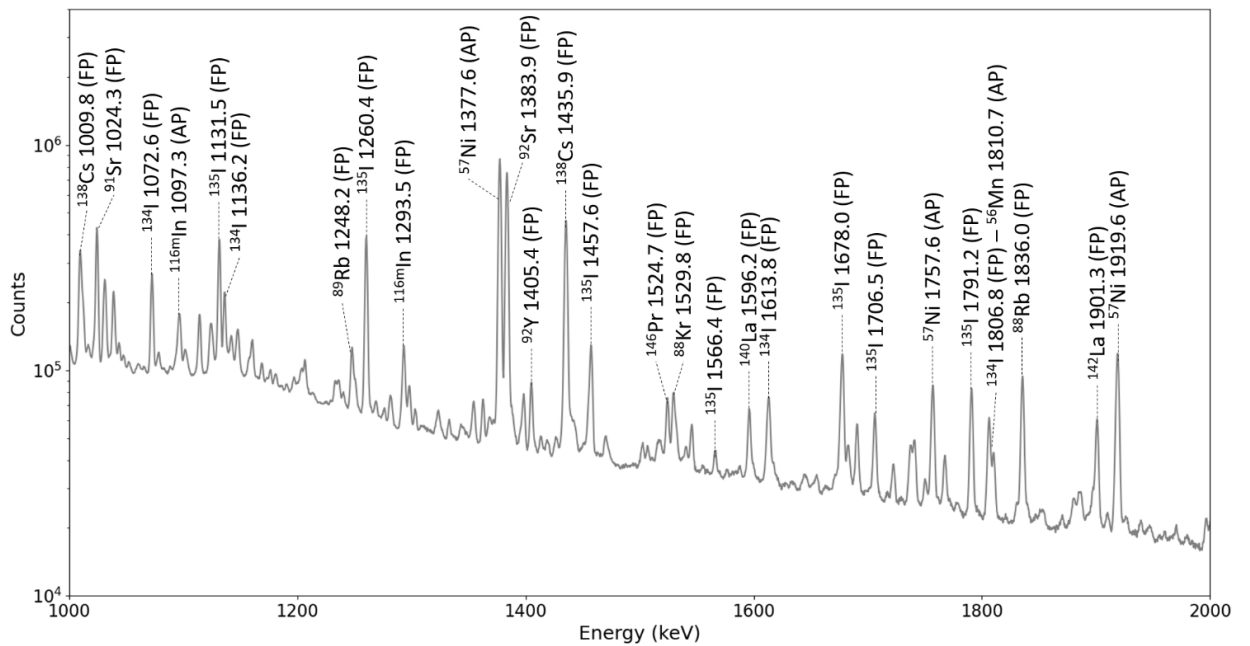


328

329

330

Figure 10: Delayed gamma spectrum of the plutonium sample (0-1000 keV) recorded during 24 h, after a 2 h irradiation and a 35 s cooling time.

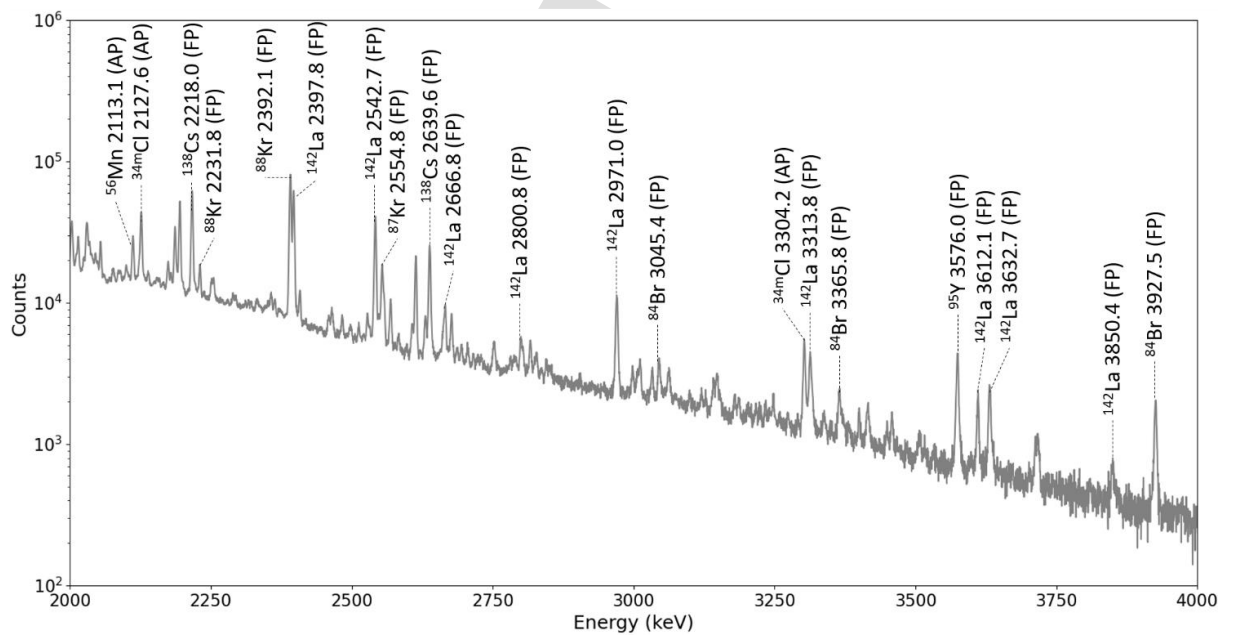


331

332

333

Figure 11: Delayed gamma spectrum of the plutonium sample (1000-2000 keV) recorded during 24 h, after a 2 h irradiation and a 35 s cooling time.



334

335

336

Figure 12: Delayed gamma spectrum of the plutonium sample (2000-4000 keV) recorded during 24 h, after a 2 h irradiation and a 35 s cooling time.

337 For all actinide samples, the delayed gamma-ray spectra have been recorded by
 338 sequences of 60 s during several dozens of hours, which allows a spectrum analysis with
 339 different cooling and measurement times to limit some interferences between close-in-
 340 energy gamma rays, by exploiting the differences in the radioactive periods of their

341 emitting isotopes (we can enhance short-lived isotopes by summing the spectra acquired
 342 shortly after irradiation, and long-lived ones latter). The spectra analysis is performed with
 343 the MAGIX software (see description in Section 2).

344 Theoretically speaking, the fission products created during irradiation are part of
 345 radioactive decay chains and their activities can be calculated by solving Bateman
 346 equations [31]. In general, these equations can be simplified by considering only the
 347 activation of the photofission product emitting the delayed gamma rays of interest, as
 348 below in (2). However, as explained further to introduce (3), it is sometimes needed to
 349 consider the direct precursor of the photofission product of interest, which are respectively
 350 called the father and daughter nuclides, like in the work of Kahane *et al.* [6] and Carrel *et*
 351 *al.* [7].

352 For a mixture of two actinides k and l , when the delayed gamma rays are emitted by a
 353 nucleus with a much longer half-life than its precursors and the cooling time, the net area
 354 $N(E_i)$ of its gamma rays of energy E_i is directly related to cumulative photofission yields
 355 $Y_{ck,p}$ and $Y_{cl,p}$ through equation (2):

$$N(E_i) = \frac{I(E_i) \varepsilon(E_i)}{\lambda_j} (1 - e^{-\lambda_j t_{irr}}) e^{-\lambda_j t_{cool}} (1 - e^{-\lambda_j t_{count}}) [\tau_p (\eta_{k,p} Y_{ck,p} + \eta_{l,p} Y_{cl,p}) + \tau_n (\eta_{k,n} Y_{ck,n} + \eta_{l,n} Y_{cl,n})] \quad (2)$$

356 With:

- 357 - $I(E_i)$ the gamma-ray intensity taken from JEFF-3.3 database [26];
- 358 - $\varepsilon(E_i)$ the absolute detection efficiency taking into account, in addition to the
 359 abovementioned intrinsic detector and geometric efficiencies, the interrogating
 360 photon flux self-shielding and delayed gamma self-attenuation in the uranium
 361 sample, both estimated with MCNP. For example, regarding the self-shielding in
 362 the DU sample, the photofission rate is 2.5 times higher on the entrance surface of
 363 the sample, with respect to the LINAC photon beam, than on its rear exit surface.
 364 Concerning self-attenuation, for instance, less than 60 % of 1 MeV delayed gamma
 365 rays emitted in the DU sample manage to escape from it;
- 366 - λ_j the radioactive decay constant of the fission product j in s^{-1} ;
- 367 - t_{irr} , t_{cool} and t_{count} respectively the irradiation, cooling and counting time, in s;
- 368 - τ_p and τ_n the photofission and neutron fission rates in the sample, in s^{-1} ;

- 369 - $Y_{ck,p}$ and $Y_{cl,p}$ the cumulative photofission yields of photofission product j ,
 370 respectively for actinides k and l (for example ^{235}U and ^{238}U);
 371 - $Y_{ck,n}$ and $Y_{cl,n}$ the cumulative fast neutron fission product yields of fission product
 372 j , respectively for actinides k and l , taken from ENDF/B-VIII.0 database [23];
 373 - $\eta_{k,p}$ and $\eta_{l,p}$ are the fractions of photofissions occurring respectively in actinides
 374 k and l , determined via MCNP simulations;
 375 - $\eta_{k,n}$ and $\eta_{l,n}$ are the fractions of neutron fissions occurring respectively in actinides
 376 k and l , determined via MCNP simulations.

377 However, when the photofission product of interest is a daughter nuclide in a decay chain
 378 with a father having a similar half-life (for instance ^{134}I and ^{138}Cs , which are respectively
 379 the daughters of ^{134}Te and ^{138}Xe , with respective radioactive periods of 41.8 and 33.4 min),
 380 net peak areas are given by (3).

$$N(E_i) = I(E_i)\varepsilon(E_i)(\tau_p[\eta_{k,p}(Y_{ik,p}^d f_d + Y_{ck,p}^f f_f) + \eta_{l,p}(Y_{il,p}^d f_d + Y_{cl,p}^f f_f)] \dots \quad (3)$$

$$\dots + \tau_n[\eta_{k,n}(Y_{ik,n}^d f_d + Y_{ck,n}^f f_f) + \eta_{l,n}(Y_{il,n}^d f_d + Y_{cl,n}^f f_f)])$$

381 Where:

- 382 - $I(E_i)$, $\varepsilon(E_i)$, τ_p , τ_n , $\eta_{k,p}$, $\eta_{l,p}$, $\eta_{k,n}$ and $\eta_{l,n}$ keep the same meaning as in (2);
 383 - $Y_{ck,p}^f$ and $Y_{cl,p}^f$ are the cumulative yields of the father nuclide, respectively for the
 384 photofission of actinides k and l ;
 385 - $Y_{ik,p}^d$ and $Y_{il,p}^d$ are the independent yields of the daughter nuclide, respectively for
 386 the photofission of actinides k and l . The independent yield (in %) of a
 387 photofission product corresponds to the number of nuclei created per 100
 388 photofissions of the considered actinide, right after the prompt neutron emission
 389 but before the delayed neutron emission. These values will be calculated to
 390 determine the cumulative photofission yield of the daughter nuclide, which is the
 391 sum of its independent yield with that of its precursor. Note that, as in Kahane *et al.*
 392 [6] and Carrel *et al.* [7], we only consider only one precursor, since the
 393 precursors of the father nuclide have a relatively short half-life compared to the
 394 cooling time of these experiments.

395 In this case, we can write $Y_{c,p}^d = Y_{i,p}^d + Y_{c,p}^f$

- 396 - $Y_{ck,n}^f$ and $Y_{cl,n}^f$ are the cumulative yields of the father nuclide, respectively for the
 397 neutron fission of actinides k and l . These values are taken from ENDF/B-VIII.0
 398 database [23];
- 399 - $Y_{ik,n}^d$ and $Y_{il,n}^d$ are the independent yields of the daughter nuclide, respectively for
 400 the neutron fission of actinides k and l . These values are taken from ENDF/B-
 401 VIII.0 database [23];
- 402 - The terms f_d and f_f describe the evolution of the respective numbers of daughter
 403 and father nuclei over time, and are given by:

$$f_d = \frac{1}{\lambda_d} (1 - e^{-\lambda_d t_{irr}}) e^{-\lambda_d t_{cool}} (1 - e^{-\lambda_d t_{count}})$$

$$f_f = \frac{1}{\lambda_d - \lambda_f} \left[\frac{\lambda_d}{\lambda_f} (1 - e^{-\lambda_f t_{irr}}) e^{-\lambda_f t_{cool}} (1 - e^{-\lambda_f t_{count}}) \dots \right. \\ \left. \dots - \frac{\lambda_f}{\lambda_d} (1 - e^{-\lambda_d t_{irr}}) e^{-\lambda_d t_{cool}} (1 - e^{-\lambda_d t_{count}}) \right]$$

404 With λ_d and λ_f the radioactive decay constants of the daughter and father nuclides
 405 (in s^{-1}), respectively, and t_{irr} , t_{cool} , t_{count} the irradiation, cooling and counting
 406 times (in s).

407 Note that when the half-life of the father nuclide is much shorter than that of the daughter
 408 nuclide, the cumulative yield of the daughter nuclide can be estimated with (2) by analyzing
 409 the delayed gamma spectrum after a cooling time equal to six times the half-life of the
 410 father nuclide (corresponding to the decay of 98.5 % of father nuclei). This approach is
 411 used in practice for the majority of fission products, the precursors of which having very
 412 short half-lives.

413 For the plutonium sample, the 1.7 % of neutron fissions (see Table 6) are subtracted to
 414 obtain the cumulative photofission yields of ^{239}Pu . Concerning the DU sample, with a ^{235}U
 415 enrichment of 0.3 %, the measured delayed gamma rays directly lead to the cumulative
 416 yields of ^{238}U photofission products, after subtraction of neutron fissions on ^{238}U that
 417 represent 5.8 % of total fissions in the sample. For the HEU sample with more than 90 %
 418 of ^{235}U , the 3.3 % of neutron fissions are subtracted to obtain the photofission rate, and the
 419 3.6 % of photofissions in ^{238}U are subtracted to calculate the cumulative yields of ^{235}U
 420 photofission products. For this purpose, we use the photofission yields obtained in this
 421 work for ^{238}U to evaluate the ^{235}U yields. For each case, the fast neutron fission yields

422 available in ENDF/B-VIII.0 database [23] are used to subtract the neutron fission
 423 contribution to the net areas of the gamma rays emitted by the fission products created in
 424 the actinide samples.

425 Finally, 26 and 28 photofission products have been identified in the spectra from their
 426 delayed gamma rays, respectively for ^{239}Pu as well as ^{235}U and ^{238}U , and their cumulative
 427 photofission yields calculated from (2) or (3). The cumulative photofission yields measured
 428 for ^{239}Pu , ^{238}U and ^{235}U are given respectively in Table 7, Table 9 and Table 11. Note that
 429 when several delayed gamma rays are measured for a photofission product, we calculate a
 430 weighted average of the cumulative yields obtained with all the peaks that are correctly
 431 processed by MAGIX software (outliers of the net areas, for instance due to interferences,
 432 are discarded). The weighting coefficient for each gamma ray is defined as the inverse of
 433 the squared relative uncertainty on the net peak area, as described in (4). Note that the
 434 weighted mean does not take into account the accuracy of the emission intensity of the
 435 considered gamma rays.

$$\bar{y}_c = \frac{\sum_{i=1}^N \frac{y_{c,i}(E_i)}{\left(\frac{\sigma(N(E_i))}{N(E_i)}\right)^2}}{\sum_{i=1}^N \frac{1}{\left(\frac{\sigma(N(E_i))}{N(E_i)}\right)^2}} \quad (4)$$

436 Where $y_{c,i}(E_i)$ is the cumulative photofission yield calculated with the net peak area $N(E_i)$
 437 of the gamma ray of energy E_i , and $\sigma(N(E_i))$ is the statistical uncertainty calculated by
 438 $\sigma(N(E_i)) = \sqrt{N(E_i) + 2B}$, with B the Compton background under this peak.

439

440 The uncertainty associated to the average cumulative yield is calculated with a quadratic
 441 propagation of the main uncertainties listed below:

- 442 - the 14.3 % uncertainty on the photofission rate in the samples (refer to section 4)
- 443 mainly due to the uncertainty on the interrogating Bremsstrahlung photon flux
- 444 (section 3). This is the largest part of the overall uncertainty, and it could be
- 445 reduced in the future by accurately measuring the (γ,n) cross-sections of the
- 446 activation materials used to characterize the photon beam, since their uncertainties
- 447 are around 10 % in EXFOR library [29];

448 - the uncertainty on the absolute detection efficiency of the gamma ray of energy E_i ,
 449 which is estimated to 7 %;

450 - the relative statistical uncertainty on the weighted average (5), $\frac{\sigma_{stat}(\bar{y}_c)}{\bar{y}_c}$, with

$$451 \quad \sigma_{stat}(\bar{y}_c) = \sqrt{\frac{1}{\sum_{i=1}^N \left(\frac{N(E_i)}{\sigma(N(E_i))} \right)^2}}.$$

452 The ^{239}Pu cumulative photofission yields measured with the plutonium sample are given
 453 in Table 7 and we provide in Table 8 all the details of the delayed gamma-ray analysis:
 454 cooling and counting times for each delayed gamma ray, energy and intensity coming from
 455 JEFF-3.3 database [26], net peak area with its associated uncertainty, and cumulative yield
 456 computed for each line. Our data (“this work”) are then compared to the values of
 457 photofission products cumulative yields previously published. Note that we report a simple
 458 average of the yields when several gamma rays are given in the other publications. The
 459 characteristics of the interrogating photon beams are indicated in the first two lines of Table
 460 7. For Bremsstrahlung photon beams, the energy indicated corresponds to the endpoint
 461 energy. The nuclides half-lives are from JEFF-3.3 database [26], except for ^{92}Sr because it
 462 is not consistent in the different databases, its half-life being taken from Leconte *et al.* [32].

463

464 *Table 7 : Cumulative yields (number of photofission products per 100 fissions) for the photofission of ^{239}Pu and*
 465 *comparison with published data*

<i>Photon beam type</i>		Bremsstrahlung	Bremsstrahlung	Bremsstrahlung	Monoenergetic	Monoenergetic
<i>Energy (MeV)</i>		17.5	28.0	22.0	11.0	13.0
Fission product	T_{1/2}	This work	Kondrat'ko 1981 [13]	Wen 2016 [11]	Bhike 2017 [14]	Krishichayan 2019 [12]
^{84}Br	31.8 min	1.19 ± 0.19	-	-	-	-
^{87}Kr	1.3 h	2.03 ± 0.32	-	-	-	1.45 ± 0.12
^{88}Kr	2.8 h	2.36 ± 0.36	1.62 ± 0.21	-	-	2.08 ± 0.15
^{89}Rb	^(a) 15.4 min	3.99 ± 0.61	-	3.45 ± 0.43	-	-
^{91}Sr	9.7 h	4.63 ± 0.72	2.89 ± 0.23	-	4.15 ± 0.51	3.91 ± 0.24
$^{91\text{m}}\text{Y}$	^(a) 49.7 min	3.19 ± 0.56	-	-	-	-
^{92}Sr	2.6 h	4.73 ± 0.76	-	4.00 ± 0.20	4.21 ± 0.49	4.19 ± 0.66
^{92}Y	3.5 h	5.42 ± 0.93	3.20 ± 0.16	-	-	-
^{93}Y	10.2 h	4.45 ± 0.58	4.02 ± 0.20	-	-	-
^{94}Y	^(a) 18.7 min	7.05 ± 1.13	-	4.60 ± 0.32	-	4.71 ± 0.33

⁹⁷ Zr	16.7 h	8.81 ± 1.41	4.63 ± 0.17	-	6.63 ± 0.73	6.78 ± 0.38
¹⁰⁴ Tc ^(a)	18.3 min	6.91 ± 1.12	-	-	-	1.96 ± 0.14
¹⁰⁵ Ru	4.4 h	6.29 ± 1.01	-	-	-	6.16 ± 0.39
¹⁰⁵ Rh	34.5 h	7.08 ± 1.11	3.96 ± 0.20	-	-	-
¹²⁸ Sn	59.1 min	1.14 ± 0.18	-	-	-	1.18 ± 0.16
¹²⁸ Sb	9 h	1.14 ± 0.19	-	-	-	-
¹²⁹ Sb	4.4 h	2.60 ± 0.42	-	-	-	2.82 ± 0.15
¹³⁰ Sb	39.5 min	1.64 ± 0.26	-	1.25 ± 0.12	-	1.36 ± 0.11
¹³¹ Sb ^(a)	23 min	2.84 ± 0.45	-	2.10 ± 0.34	-	-
¹³⁴ Te	41.8 min	4.88 ± 0.78	-	11.6 ± 0.81	-	-
¹³⁴ I	52.5 min	7.02 ± 1.16	-	5.90 ± 0.15	7.39 ± 0.89	-
¹³⁵ I	6.6 h	5.67 ± 0.94	-	-	-	-
¹³⁸ Cs	33.4 min	8.24 ± 1.33	-	5.50 ± 0.29	6.18 ± 0.75	6.45 ± 0.37
¹⁴¹ Ba ^(a)	18.3 min	7.28 ± 1.20	-	-	-	4.22 ± 0.31
¹⁴² La	1.5 h	6.27 ± 1.00	-	4.90 ± 0.29	-	5.87 ± 0.31
¹⁴³ Ce	1.4 d	4.48 ± 0.76	3.26 ± 0.13	-	4.41 ± 0.51	3.88 ± 0.20

^(a)Results obtained with the measurement referred to as Pu 2 in Table 3 and Figure 5. The other cumulative photofission yields of ²³⁹Pu are obtained with the Pu 1 measurement.

466

467

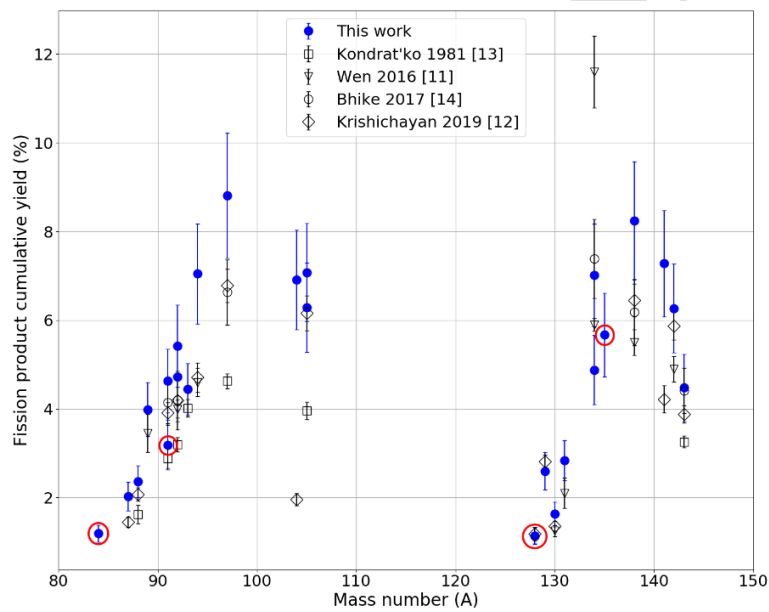
Table 8: Detailed data of the delayed gamma-ray analysis for each ²³⁹Pu photofission product

Fission Product	Cooling time	Counting time	Gamma-ray energy (keV)	Relative intensity (%)	Net peak area (counts)	Photofission cumulative yield (%)
⁸⁴ Br	50.1 min	2.3 h	1897.60	14.56	24858 ± 312	1.23
			1015.90	6.16	18493 ± 565	1.46
			2484.10	6.66	7682 ± 164	1.01
			3927.50	6.78	5977 ± 79	1.16
			1463.80	1.96	3631 ± 357	1.13
⁸⁷ Kr	50.1 min	6.8 h	402.59	49.60	958383 ± 1801	2.00
			2554.80	9.23	74263 ± 308	2.17
			2558.10	3.92	31501 ± 229	2.17
⁸⁸ Kr	50.1 min	16.2 h	196.30	25.98	547139 ± 2605	2.23
			2392.11	34.60	525449 ± 752	2.31
			834.83	12.97	426400 ± 1122	2.64
			1529.77	10.93	224744 ± 660	2.28
			2195.84	13.18	222652 ± 544	2.40
			2029.84	4.53	80749 ± 413	2.39
			2035.41	3.74	66486 ± 394	2.39
			2231.77	3.39	51489 ± 342	2.19
1518.39	2.15	44384 ± 508	2.28			
⁸⁹ Rb	9.5 min	1.7 h	1032.00	63.60	30790 ± 352	3.80
			1248.20	45.60	21750 ± 277	4.24
			657.80	11.00	7528 ± 523	4.24
			2570.10	10.18	2629 ± 82	3.81
⁹¹ Sr	1.8 h	22.9 h	1024.30	33.50	1799550 ± 1512	4.50
			749.80	23.68	1580910 ± 1540	4.86
			652.90	8.04	510024 ± 1294	4.33

			652.30	2.98	189136 ± 1163	4.33
^{91m} Y	9.5 min	20.4 h	555.57	95.00	302322 ± 923	3.19
⁹² Sr	1.8 h	22.9 h	1383.90	93.00	3168600 ± 1831	4.74
			953.30	3.62	148282 ± 809	4.64
			1142.39	2.86	108084 ± 785	4.70
⁹² Y	1.8 h	22.9 h	934.50	13.90	1140370 ± 1291	5.42
⁹³ Y	1.8 h	22.9 h	266.90	7.42	406743 ± 2240	3.64
			947.10	2.12	137801 ± 806	5.35
			680.20	0.67	45512 ± 1029	4.79
⁹⁴ Y	9.5 min	1.8 h	918.74	56.00	70359 ± 1167	7.05
⁹⁷ Zr	1.8 h	22.9 h	1147.97	2.62	211786 ± 796	8.81
¹⁰⁴ Tc	9.5 min	2.1 h	535.10	14.69	22763 ± 609	7.00
			884.40	10.95	12685 ± 394	6.44
			893.10	10.23	13116 ± 394	7.18
			1676.80	7.83	6592 ± 196	7.12
			1612.40	5.79	4632 ± 199	6.59
¹⁰⁵ Ru	1.8 h	22.9 h	724.30	47.30	3994660 ± 2209	6.30
			469.37	17.55	1727880 ± 2019	6.22
			676.36	15.66	1365110 ± 1557	6.30
			316.44	11.12	1076530 ± 2253	6.06
			393.36	3.78	383858 ± 1781	6.22
			875.85	2.50	211630 ± 895	6.93
¹⁰⁵ Rh	1.8 h	22.9 h	969.44	2.11	164478 ± 813	6.66
			318.90	19.10	1045508 ± 2234	7.07
¹⁰⁵ Rh	1.8 h	22.9 h	306.10	5.10	285966 ± 2103	7.28
¹²⁸ Sn	50.1 min	5.1 h	482.30	59.00	483730 ± 1472	1.14
¹²⁸ Sb	1.8 h	22.9 h	314.10	61.00	1233351 ± 2298	1.20
			754.00	100.00	1639830 ± 1557	1.18
			636.20	36.00	457603 ± 1144	0.86
			628.70	31.00	415906 ± 2162	0.91
¹²⁹ Sb	1.8 h	22.9 h	812.80	47.60	1586460 ± 1505	2.66
			914.50	20.94	584657 ± 1065	2.36
			760.80	3.33	114663 ± 934	2.66
			772.80	3.05	104078 ± 911	2.66
			876.00	2.86	81428 ± 819	2.36
¹³⁰ Sb	50.1 min	3.1 h	793.40	100.00	549107 ± 1050	1.63
			330.91	78.00	569154 ± 1592	1.72
			839.52	100.00	533861 ± 1023	1.63
			182.33	65.00	204834 ± 1730	1.52
			732.00	22.00	100176 ± 888	1.30
¹³¹ Sb	9.5 min	2.1 h	943.40	46.20	29222 ± 394	2.78
			933.10	25.87	17640 ± 382	2.98
¹³⁴ Te	50.1 min	3.3 h	277.95	21.30	411731 ± 1685	4.88
			201.24	8.90	123133 ± 1767	4.92
¹³⁴ I	50.1 min	8.6 h	857.29	6.70	432668 ± 1051	7.21
			1613.80	4.31	177159 ± 583	6.50
			1741.49	2.57	107325 ± 487	7.34
¹³⁵ I	1.8 h	22.9 h	1260.41	28.70	1844600 ± 1454	5.87
			1131.51	22.59	1416620 ± 1386	5.40
			1038.76	7.95	552762 ± 1017	5.69
			836.80	6.69	476552 ± 1059	5.27
			1678.03	9.56	497395 ± 781	5.65
			1457.56	8.67	499735 ± 818	5.75
			1791.20	7.72	394075 ± 690	5.80
			1124.00	3.62	227641 ± 847	5.40
1706.46	4.10	211984 ± 563	5.67			
¹³⁸ Cs	50.1 min	4.7 h	1435.86	76.30	1214440 ± 1177	8.32
			1009.78	29.83	568411 ± 991	7.97
			2218.00	15.18	178761 ± 486	8.32
			871.8	5.11	103228 ± 795	7.77

			2639.59	7.63	77034 ± 304	8.12
^{141}Ba	9.5 min	1.7 h	739.20	4.83	6597 ± 467	7.07
			625.40	3.59	5681 ± 529	7.64
^{142}La	50.1 min	9.3 h	641.29	47.40	3033430 ± 2131	6.28
			894.90	8.34	460260 ± 1040	6.33
			1901.30	7.16	230758 ± 578	5.99
			1011.40	3.93	202468 ± 856	6.34
			1043.70	2.70	135455 ± 805	6.29
^{143}Ce	1.8 h	22.9 h	293.27	42.80	1816230 ± 2477	4.78
			350.62	3.23	144406 ± 1899	4.78
			231.55	2.05	59502 ± 2382	4.08
			880.46	1.03	34612 ± 787	4.82

468 Our photofission products cumulative yields data for ^{239}Pu are compared in Figure 13 to
 469 already published data.



470

471 *Figure 13: Fission product yields distribution for the photofission of ^{239}Pu and comparison with existing data.*

472 In this work, we provide the cumulative photofission yields of ^{239}Pu fission products ^{84}Br ,
 473 $^{91\text{m}}\text{Y}$, ^{128}Sb and ^{135}I that were not published before (circled points in Figure 13). We can
 474 note that relative yields were recently published by Parlag *et al.* [33] for ^{135}I and $^{91\text{m}}\text{Y}$ for
 475 a 17.5 MeV Bremsstrahlung endpoint energy, but in this paper, all yields are normalized
 476 to that of ^{97}Zr published by Kondrat'ko *et al.* [13] (first dataset published in 1981
 477 concerning the photofission yields of ^{239}Pu), which is significantly lower than other
 478 published data and particularly our work, see Table 7. More globally, the photofission
 479 yields provided in our work are a little larger but consistent with the other data. We can
 480 note a few singular points like the ^{104}Tc yield from Krishichayan *et al.* [12], $1.96 \pm 0.14 \%$,

481 which is much lower than expected for this mass number. Our work gives 6.91 ± 1.12 %
 482 and for comparison, the neutron fission yield is 5.69 % from ENDF/B-VIII.0 database [23].
 483 We can also mention that Kondrat'ko *et al.* data [13] are globally low and some points
 484 also appear as singular, such as the yield of ^{105}Rh , 3.96 ± 0.20 %, compared to our
 485 measurement, 7.08 ± 1.11 %, and to the yields of ^{105}Ru with the same atomic number (near
 486 6 %). The yield of ^{134}Te from Wen *et al.* [11] also looks like an outlier with 11.6 ± 0.81 %,
 487 compared to our data 4.88 ± 0.78 % and to ^{134}I with this atomic number (near 6-7 %).
 488 Except for the singular data mentioned above, the observed discrepancies in the published
 489 photofission yields is probably due, for a significant part, to the different experimental
 490 configurations (geometry of the samples, energy spectrum and intensity of the interrogating
 491 photon beams, photoneutron production, irradiation-cooling-counting times, detectors,
 492 etc.) and possibly to data analysis (subtraction of neutron fissions, gamma-ray
 493 interferences, decay chain calculations to take into account precursors, etc.). In our case,
 494 analyzing several gamma-ray lines for a same photofission product (when possible, for
 495 example ^{87}Kr , ^{88}Kr , ^{134}I , ^{135}I , ^{138}Cs , ^{142}La) and observing a good consistency in the different
 496 yields associated with each line improves the confidence of the weighted average reported
 497 as cumulative yield. It is also important to mention that our results share a common
 498 uncertainty of 14 % related to the photon flux assessment. In addition, our plutonium
 499 sample is not exclusively made of ^{239}Pu , the photofission yields of the other actinides
 500 composing it (^{240}Pu , ^{242}Pu , ^{241}Am) should be investigated with as pure as possible samples
 501 in order to evaluate the contribution of each isotope.

502
 503 The ^{238}U cumulative photofission yields measured with the DU sample are given in Table
 504 9, and the details of the delayed gamma-ray analysis in Table 10.

505 *Table 9: Cumulative yields (number of photofission products per 100 fissions) for the photofission of ^{238}U and*
 506 *comparison with published data*

Photon beam type		Bremsstrahlung	Bremsstrahlung	Neutron-capture gamma rays	Bremsstrahlung	Bremsstrahlung	Bremsstrahlung	Bremsstrahlung	Bremsstrahlung	Monoenergetic
Energy (MeV)		17.5	15.8	7.8	16.3	10.0	14.987	8.0	22.0	13.0
Fission Product	$T_{1/2}$	This work	Our previous work [19]	Kahane 1985 [6]	Carrel 2011 [7]	Naik 2011 [8]	Naik 2013 [9]	Naik 2014 [10]	Wen 2016 [11]	Krishichayan 2019 [12]
^{84}Br	31.8 min	1.01 ± 0.16	1.37 ± 0.20	-	-	-	0.90 ± 0.06	0.30 ± 0.06	-	2.49 ± 0.19
^{87}Kr	1.3 h	1.90 ± 0.29	1.96 ± 0.31	1.82 ± 0.21	-	1.61 ± 0.20	1.86 ± 0.30	1.11 ± 0.13	1.0 ± 0.06	2.29 ± 0.16
^{88}Kr	2.8 h	2.35 ± 0.38	2.24 ± 0.34	-	2.52 ± 0.23	2.77 ± 0.53	2.58 ± 0.19	2.77 ± 0.38	1.0 ± 0.03	2.92 ± 0.17
^{89}Rb	15.4 min	3.44 ± 0.55	3.50 ± 0.55	2.51 ± 0.40	3.30 ± 0.20	-	3.12 ± 0.16	3.42 ± 0.34	1.4 ± 0.13	-

⁹¹ Sr	9.7 h	3.93 ± 0.64	3.86 ± 0.60	3.81 ± 0.45	4.53 ± 0.22	3.82 ± 0.17	3.69 ± 0.23	4.75 ± 0.48	-	5.27 ± 0.18
⁹² Sr	2.6 h	4.09 ± 0.66	4.04 ± 0.63	-	4.77 ± 0.22	3.83 ± 0.45	4.26 ± 0.13	4.59 ± 0.47	1.7 ± 0.02	4.82 ± 0.15
⁹⁴ Y	18.7 min	4.87 ± 0.79	4.48 ± 0.77	-	5.06 ± 0.24	-	4.47 ± 0.25	4.25 ± 0.47	-	7.50 ± 0.46
⁹⁷ Zr	16.7 h	5.82 ± 0.94	5.95 ± 0.93	5.89 ± 0.66	-	5.43 ± 0.19	5.78 ± 0.17	6.00 ± 0.64	-	6.20 ± 0.19
⁹⁹ Mo	2.7 d	6.01 ± 0.97	4.65 ± 0.77	-	-	4.84 ± 0.44	5.11 ± 0.15	4.75 ± 0.50	-	6.57 ± 0.22
¹⁰¹ Mo	14.6 min	6.56 ± 1.09	5.37 ± 0.86	-	6.78 ± 0.32	-	7.13 ± 0.30	7.56 ± 0.77	-	-
¹⁰⁴ Tc	18.3 min	3.80 ± 0.63	3.60 ± 0.56	4.13 ± 0.50	-	-	3.65 ± 0.28	4.06 ± 0.42	-	4.44 ± 0.64
¹⁰⁵ Ru	4.4 h	2.78 ± 0.46	2.76 ± 0.44	2.95 ± 0.45	-	2.57 ± 0.21	2.55 ± 0.06	2.91 ± 0.38	-	4.06 ± 0.20
¹²⁸ Sn	59.1 min	0.58 ± 0.09	0.57 ± 0.09	-	-	-	0.85 ± 0.04	0.21 ± 0.03	-	1.22 ± 0.22
¹²⁸ Sb	9 h	0.22 ± 0.04	0.21 ± 0.03	-	0.16 ± 0.01	-	-	-	-	-
¹²⁹ Sb	4.4 h	1.24 ± 0.20	1.09 ± 0.17	0.54 ± 0.10	1.33 ± 0.06	1.48 ± 0.33	1.35 ± 0.16	0.63 ± 0.06	-	2.59 ± 0.09
¹³⁰ Sb	39.5 min	0.89 ± 0.14	0.79 ± 0.12	-	1.08 ± 0.05	-	-	-	-	1.61 ± 0.11
¹³¹ Sb	23 min	2.65 ± 0.43	2.51 ± 0.37	-	3.94 ± 0.19	-	4.18 ± 0.18	2.40 ± 0.27	-	5.01 ± 0.33
^{131m} Te	1.3 d	0.86 ± 0.14	0.70 ± 0.10	3.12 ± 0.40	-	-	-	-	-	-
¹³² Te	3.2 d	4.71 ± 0.77	4.71 ± 0.73	2.43 ± 0.50	-	4.84 ± 0.46	5.48 ± 0.14	6.15 ± 0.65	-	5.44 ± 0.25
¹³² I	2.3 h	4.72 ± 0.79	4.87 ± 0.76	3.74 ± 0.46	-	-	-	-	-	-
^{133m} Te	55.4 min	3.19 ± 0.51	3.23 ± 0.44	2.35 ± 0.39	4.43 ± 0.21	-	-	-	3.8 ± 0.42	-
¹³⁴ Te	41.8 min	5.58 ± 0.92	5.29 ± 0.84	6.25 ± 0.89	6.34 ± 0.30	8.27 ± 0.26	7.23 ± 0.33	7.21 ± 0.74	-	7.43 ± 0.51
¹³⁴ I	52.5 min	7.00 ± 1.25	7.30 ± 1.16	6.29 ± 0.94	-	-	8.06 ± 0.34	8.63 ± 0.87	3.1 ± 0.19	-
¹³⁵ I	6.6 h	5.75 ± 0.95	5.85 ± 0.92	5.91 ± 0.68	6.66 ± 0.42	5.88 ± 0.57	5.57 ± 0.12	6.55 ± 0.67	2.6 ± 0.16	6.13 ± 0.29
¹³⁸ Xe	14.1 min	5.59 ± 0.90	3.75 ± 0.59	5.38 ± 0.90	6.60 ± 0.58	-	-	5.91 ± 0.63	1.8 ± 0.41	-
¹³⁸ Cs	33.4 min	5.87 ± 1.11	5.91 ± 0.86	6.10 ± 0.71	-	8.00 ± 0.48	6.84 ± 0.25	6.44 ± 0.68	2.6 ± 0.10	-
¹⁴¹ Ba	18.3 min	5.48 ± 0.86	4.75 ± 0.73	-	-	-	4.51 ± 0.23	5.44 ± 0.56	-	-
¹⁴² La	1.5 h	4.74 ± 0.79	4.89 ± 0.88	3.69 ± 0.43	5.01 ± 0.24	5.26 ± 0.52	4.69 ± 0.20	4.88 ± 0.52	1.7 ± 0.13	5.58 ± 0.18

507

508

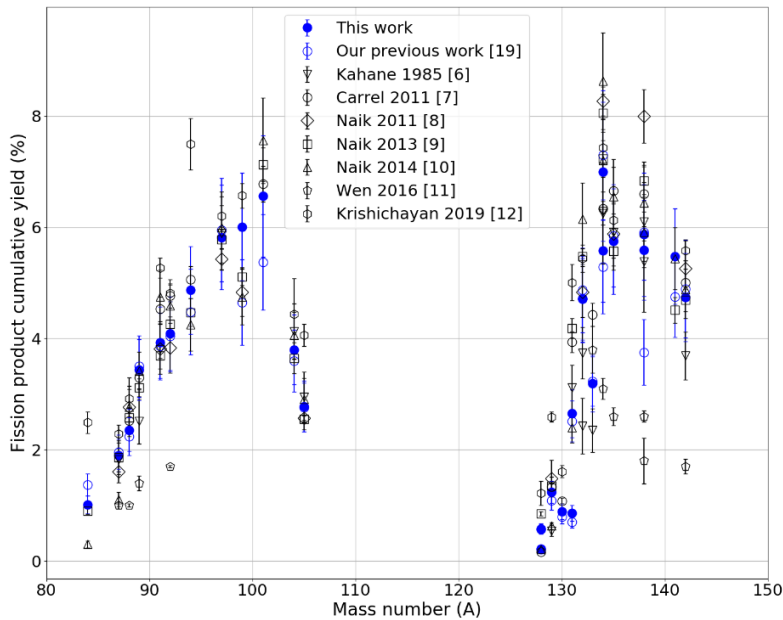
Table 10: Detailed data of the delayed gamma-ray analysis for each ²³⁸U photofission product

Fission Product	Cooling time	Counting time	Gamma-ray energy (keV)	Relative intensity (%)	Net peak area (counts)	Photofission cumulative yield (%)
⁸⁴ Br	20.0 min	3.2 h	881.60	41.60	72262 ± 695	0.88
			1897.60	14.56	24041 ± 318	0.95
			1015.90	6.16	13767 ± 562	1.13
			802.20	5.99	9578 ± 723	0.82
			2484.10	6.66	10377 ± 173	1.03
			3927.50	6.78	8729 ± 95	1.20
			3365.80	2.87	3461 ± 78	0.99
3235.30	2.04	2452 ± 77	0.95			
⁸⁷ Kr	19.0 min	7.6 h	402.59	49.60	250860 ± 1359	1.79
			2554.80	9.23	60419 ± 281	1.97
			2558.10	3.92	25636 ± 211	1.97
			2011.88	2.88	19727 ± 313	1.79
⁸⁸ Kr	19.0 min	16.7 h	2392.11	34.60	400897 ± 659	2.34
			834.83	12.97	191623 ± 938	2.39
			1529.77	10.93	159206 ± 571	2.42
			2029.84	4.53	58502 ± 374	2.39
			2035.41	3.74	48190 ± 358	2.39
			2231.77	3.39	39608 ± 314	2.26

			1518.39	2.15	31391 ± 456	2.42
⁸⁹ Rb	19.0 min	1.7 h	1032.00	63.60	149511 ± 623	3.43
			1248.20	45.60	106176 ± 516	3.44
			657.80	11.00	23747 ± 801	3.47
			2570.10	10.18	17964 ± 177	3.47
⁹¹ Sr	19.0 min	41.6 h	1024.30	33.50	1025360 ± 1223	3.97
			749.80	23.68	666694 ± 1258	3.83
⁹² Sr	19.0 min	16.7 h	1383.90	93.00	2317890 ± 1589	4.09
⁹⁴ Y	19.0 min	1.9 h	918.74	56.00	260995 ± 1461	4.87
			550.9	4.93	19427 ± 892	4.94
⁹⁷ Zr	19.0 min	41.6 h	1149.97	2.62	105437 ± 705	5.83
			1750.24	1.09	39384 ± 399	5.78
⁹⁹ Mo	19.0 min	41.6 h	739.50	12.12	215280 ± 1085	6.01
¹⁰¹ Mo	19.0 min	1.4 h	590.10	19.21	69639 ± 824	6.76
			1012.47	13.02	52392 ± 524	6.49
			1532.49	6.14	23139 ± 337	6.40
¹⁰⁴ Tc	19.0 min	1.9 h	358.00	89.00	178773 ± 1124	3.87
			535.10	14.69	40712 ± 913	3.57
			893.10	10.23	32790 ± 599	3.37
			1596.70	4.18	14101 ± 332	3.80
			1157.40	2.85	11038 ± 479	4.10
			2123.80	2.23	6507 ± 241	3.70
¹⁰⁵ Ru	19.0 min	26.2 h	724.30	47.30	919049 ± 1370	2.81
			676.36	15.66	275906 ± 1169	2.59
			469.37	17.55	260961 ± 1454	2.76
¹²⁸ Sn	19.0 min	5.6 h	482.30	59.00	93194 ± 1186	0.58
¹²⁸ Sb	1.5 h	40.4 h	754.00	100.00	141414 ± 801	0.22
¹²⁹ Sb	19.0 min	26.2 h	812.80	47.60	403876 ± 1076	1.24
			544.70	18.09	141730 ± 1277	1.36
			966.50	8.14	66692 ± 746	1.16
			683.50	5.66	44137 ± 1051	1.19
¹³⁰ Sb	1.0 h	3.0 h	839.52	100.00	103362 ± 624	0.85
			793.40	100.00	109564 ± 652	0.92
			330.91	78.00	43614 ± 946	0.92
			732.00	22.00	21619 ± 634	0.84
¹³¹ Sb	19.0 min	1.9 h	943.40	46.20	162988 ± 677	2.66
			933.10	25.87	90233 ± 626	2.63
			1207.40	3.88	13656 ± 458	2.66
			2335.00	1.85	4798 ± 191	2.45
^{131m} Te	19.0 min	41.6 h	852.21	21.40	90922 ± 897	0.86
¹³² Te	40.2 min	41.3 h	228.33	88.12	301254 ± 8404	4.71
¹³² I	19.0 min	41.6 h	667.71	98.7	1128590 ± 1521	4.72
^{133m} Te	19.0 min	7.6 h	912.67	55.27	633754 ± 1055	3.17
			647.51	19.40	208071 ± 1112	3.25
			863.96	15.64	181664 ± 862	3.25
			914.77	10.94	123117 ± 772	3.10
¹³⁴ Te	19.0 min	3.9 h	767.20	29.60	448907 ± 1026	5.67
			565.99	18.60	230043 ± 1096	5.22
			277.95	21.30	123853 ± 1307	5.49
			464.64	5.03	54548 ± 1119	5.32
¹³⁴ I	19.0 min	9.2 h	884.09	65.08	2484463 ± 1738	6.95
			1136.16	9.09	364607 ± 843	7.36
			540.83	7.66	252969 ± 1237	7.49
			1613.80	4.31	159594 ± 543	7.32
¹³⁵ I	19.0 min	38.9 h	1260.41	28.70	1282530 ± 1250	5.86
			1131.51	22.59	919069 ± 1151	5.22
			1678.03	9.56	410034 ± 736	6.06
			1457.56	8.67	388947 ± 768	6.07
			1038.76	7.95	352406 ± 900	5.72
			1791.20	7.72	312318 ± 652	5.83

			836.80	6.69	298895 ± 1021	5.95
			1706.46	4.10	175261 ± 549	6.06
			1124.00	3.62	147227 ± 746	5.22
^{138}Xe	19.0 min	1.4 h	1768.26	16.73	49177 ± 340	5.59
^{138}Cs	19.0 min	4.4 h	462.80	30.75	431772 ± 1294	5.83
			871.80	5.11	100812 ± 759	6.13
			408.98	4.66	58254 ± 1179	5.87
^{141}Ba	19.0 min	1.4 h	304.19	25.44	53238 ± 1030	5.28
			343.67	14.44	37741 ± 988	5.60
			739.20	4.83	23791 ± 682	5.78
^{142}La	19.0 min	9.2 h	641.29	47.40	743908 ± 1202	4.93
			2397.80	13.27	156821 ± 415	4.26
			894.90	8.34	134809 ± 672	4.60
			1901.30	7.16	105968 ± 397	4.78
			1011.40	3.93	66289 ± 560	4.76
			2055.20	2.18	31017 ± 274	4.76
			3313.80	0.95	9499 ± 104	4.55

509 Our fission products cumulative yields for ^{238}U are compared in Figure 14 to other existing
 510 data.



511

512

Figure 14: Fission product yields distribution for the photofission of ^{238}U and comparison with existing data.

513

514

515

516

517

518

519

The values provided for the cumulative photofission yields of ^{238}U through this experimental campaign confirm the results obtained in our previous work [19]. No significant difference of the photofission yields is observed between the 15.8 MeV and 17.5 MeV electron endpoint energy, except that of ^{138}Xe for which counting statistics was greatly improved in our new measurement, allowing to refine this yield (and in the same way for ^{101}Mo , to a lesser extent). Wen *et al.* [11] data seem to show a systematic bias and are mostly below the expected values for the different mass numbers of the reported

520 photofission products. The yield of ^{94}Y from Krishichayan *et al.* [12] also looks like an
 521 outlier with $7.50 \pm 0.46 \%$, compared to our data $4.87 \pm 0.79 \%$, which is coherent with
 522 all the other datasets displayed.

523

524 The ^{235}U cumulative photofission yields measured with the HEU sample are given in Table 11
 525 and the details of gamma analysis in
 526 Table 12.

527
 528

Table 11: Cumulative yields (number of photofission products per 100 fissions) for the photofission of ^{235}U and comparison with published data

<i>Photon beam type</i>		Bremsstrahlung	Bremsstrahlung	Bremsstrahlung	Monoenergetic
<i>Energy (MeV)</i>		17.5	15.8	16.3	13.0
Fission product	T_{1/2}	This work	Our previous work [19]	Carrel 2011 [7]	Krishichayan 2019 [12]
^{84}Br	31.8 min	1.71 ± 0.30	-	-	1.77 ± 0.13
^{87}Kr	1.3 h	3.07 ± 0.53	4.64 ± 0.74	-	3.45 ± 0.28
^{88}Kr	2.8 h	3.59 ± 0.59	5.34 ± 0.84	3.63 ± 0.32	3.87 ± 0.22
^{89}Rb	15.4 min	4.76 ± 0.82	6.89 ± 1.08	4.69 ± 0.28	-
^{91}Sr	9.7 h	4.62 ± 0.82	7.71 ± 1.18	5.37 ± 0.26	6.08 ± 0.26
^{92}Sr	2.6 h	5.17 ± 0.90	7.92 ± 1.24	5.59 ± 0.26	6.52 ± 0.21
^{94}Y	18.7 min	6.03 ± 1.04	-	5.81 ± 0.27	6.84 ± 0.37
^{99}Mo	16.7 h	4.28 ± 0.77	-	-	5.32 ± 0.20
^{101}Mo	14.6 min	5.43 ± 0.96	-	4.19 ± 0.20	-
^{104}Tc	18.3 min	1.99 ± 0.36	1.52 ± 0.24	-	2.37 ± 0.14
^{105}Ru	4.4 h	1.28 ± 0.23	1.86 ± 0.29	-	1.90 ± 0.11
^{128}Sn	59.1 min	0.96 ± 0.16	1.38 ± 0.22	-	1.22 ± 0.16
^{129}Sb	4.4 h	1.67 ± 0.28	2.46 ± 0.36	1.60 ± 0.08	2.47 ± 0.12
^{130}Sb	39.5 min	1.12 ± 0.19	1.49 ± 0.25	1.12 ± 0.05	0.82 ± 0.06
^{131}Sb	23 min	2.03 ± 0.37	3.42 ± 0.53	2.75 ± 0.13	1.59 ± 0.13
$^{131\text{m}}\text{Te}$	1.3 d	1.15 ± 0.17	1.98 ± 0.33	-	-
^{132}Te	3.2 d	4.57 ± 0.80	-	-	4.98 ± 0.26
^{132}I	2.3 h	4.89 ± 0.86	-	-	-
$^{133\text{m}}\text{Te}$	55.4 min	3.18 ± 0.55	-	4.21 ± 0.20	-
^{134}Te	41.8 min	4.12 ± 0.74	5.33 ± 0.84	3.16 ± 0.15	5.37 ± 0.39
^{134}I	52.5 min	5.00 ± 1.87	7.52 ± 2.22	-	-
^{135}I	6.6 h	4.72 ± 0.85	7.34 ± 1.14	5.06 ± 0.32	4.72 ± 0.21
^{138}Xe	14.1 min	4.35 ± 0.78	7.36 ± 1.18	4.62 ± 0.41	-

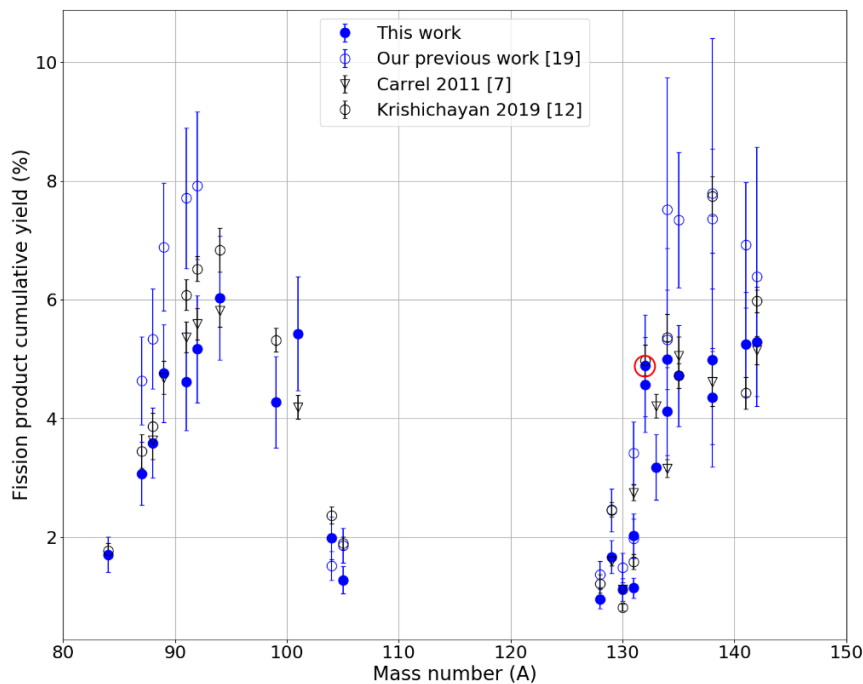
¹³⁸ Cs	33.4 min	4.99 ± 1.80	7.79 ± 2.61	-	7.74 ± 0.33
¹⁴¹ Ba	18.3 min	5.25 ± 0.88	6.92 ± 1.06	-	4.43 ± 0.27
¹⁴² La	1.5 h	5.29 ± 0.92	6.39 ± 2.18	5.15 ± 0.24	5.98 ± 0.19

529
530Table 12: Detailed data of the delayed gamma-ray analysis for each ²³⁵U photofission product

Fission Product	Cooling time	Counting time	Gamma-ray energy (keV)	Relative intensity (%)	Net peak area (counts)	Photofission cumulative yield (%)
⁸⁴ Br	19.9 min	2.8 h	881.60	41.60	27836 ± 387	1.79
			2484.10	6.66	2322 ± 84	1.48
			3927.50	6.78	1765 ± 42	1.56
⁸⁷ Kr	5.8 min	7.5 h	402.59	49.60	178305 ± 914	3.09
			2554.80	9.23	16155 ± 149	2.96
			2558.10	3.92	7386 ± 116	3.20
			2011.88	2.88	5792 ± 182	2.95
⁸⁸ Kr	42 s	17.0 h	196.30	25.98	102192 ± 1261	3.46
			834.83	12.97	60791 ± 570	3.48
			1529.77	10.93	34211 ± 325	3.71
			2231.77	3.39	10623 ± 184	3.55
⁸⁹ Rb	16.9 min	1.8 h	1248.20	45.60	28161 ± 258	4.80
			2570.10	10.18	4169 ± 85	4.58
⁹¹ Sr	5.8 min	23.8 h	1024.30	33.50	194351 ± 588	4.68
			749.80	23.68	146727 ± 674	4.47
			925.8	3.85	23247 ± 462	4.68
⁹² Sr	42 s	17.0 h	1383.90	93.00	532609 ± 778	5.17
⁹⁴ Y	7.8 min	1.8 h	918.74	56.00	93343 ± 448	6.03
			1138.9	5.99	9275 ± 271	6.03
⁹⁹ Mo	9.8 min	23.8 h	739.50	12.12	21083 ± 571	4.24
			777.92	4.28	7828 ± 530	4.56
¹⁰¹ Mo	42 s	1.4 h	1012.47	13.02	19380 ± 432	5.43
¹⁰⁴ Tc	5.8 min	2.1 h	358.00	89.00	67074 ± 763	2.00
			1596.70	4.18	1782 ± 188	1.71
			3149.20	1.16	334 ± 35	1.74
¹⁰⁵ Ru	46.2 min	23.2 h	724.30	47.30	85493 ± 557	1.28
			676.36	15.66	29663 ± 534	1.31
			316.44	11.12	23348 ± 897	1.32
¹²⁸ Sn	42 s	5.9 h	482.30	59.00	56919 ± 796	0.93
			680.50	15.93	16847 ± 590	1.12
¹²⁹ Sb	1.5 h	22.4 h	812.80	47.60	114447 ± 637	1.67
			544.70	18.09	49999 ± 766	1.71
¹³⁰ Sb	1.0 h	2.9 h	793.40	100.00	26825 ± 361	1.10
			839.52	100.00	26971 ± 346	1.13
¹³¹ Sb	5.8 min	2.1 h	943.40	46.20	36721 ± 387	2.08
			933.10	25.87	18752 ± 366	1.87
^{131m} Te	42 s	23.9 h	852.21	21.40	14450 ± 527	1.00
			1125.44	11.90	9653 ± 380	1.33
¹³² Te	40.1 min	23.3 h	228.33	88.12	129579 ± 1055	4.57
¹³² I	42 s	23.9 h	667.71	98.70	189532 ± 779	4.89
			522.65	15.99	32271 ± 782	4.87
			630.19	13.32	26635 ± 693	4.93
^{133m} Te	42 s	8.0 h	912.67	55.27	151897 ± 584	3.13
			647.51	19.40	61265 ± 665	3.23
			863.96	15.64	43916 ± 520	3.14
			978.30	4.86	13696 ± 411	3.30
¹³⁴ Te	42 s	4.1 h	767.20	29.60	95959 ± 587	4.12
¹³⁴ I	42 s	9.4 h	884.09	65.08	413068 ± 789	5.00
			1072.55	14.93	88376 ± 471	5.00

			595.36	11.10	78034 ± 708	4.87
^{135}I	42 s	23.9 h	1260.41	28.70	176093 ± 518	4.80
			1131.51	22.59	134550 ± 516	4.44
			1038.76	7.95	48496 ± 460	4.43
			1678.03	9.56	52684 ± 322	4.92
			1457.56	8.67	52650 ± 352	5.09
^{138}Xe	42 s	1.4 h	1768.26	16.73	15536 ± 246	4.34
			258.41	31.50	43390 ± 1181	4.39
^{138}Cs	42 s	4.7 h	1435.86	76.30	271157 ± 573	4.99
			1009.78	29.38	122123 ± 506	5.03
			2218.00	15.18	42828 ± 255	4.87
^{141}Ba	2.7 min	1.7 h	190.328	46.00	62679 ± 942	4.98
			304.19	25.44	54247 ± 828	5.37
			276.95	23.41	48450 ± 836	5.43
			343.67	14.44	30891 ± 758	5.28
^{142}La	1.1 h	8.7 h	641.29	47.4	189460 ± 632	5.30
			894.90	8.34	30424 ± 362	5.37
			1901.30	7.16	18446 ± 188	5.17
			2187.20	3.70	9598 ± 146	5.65
			2971.00	3.13	5885 ± 80	4.97
			2055.20	2.18	5271 ± 136	5.04

531 Our fission products cumulative yields for ^{235}U are compared in Figure 15 to existing
 532 published data.



533

534

Figure 15: Fission product yields distribution for the photofission of ^{235}U and comparison with existing data.

535

536

537

Contrary to our previous work [19], we were not able to measure the cumulative yields of some short half-life photofission products (like ^{93}Sr or ^{142}Ba , with respective radioactive periods of 7.4 min and 10.6 min) because of the dead time issues mentioned in section 2.

538 However, we measured new yields (^{84}Br , $^{91\text{m}}\text{Y}$, ^{99}Mo , ^{101}Mo , ^{132}Te , ^{132}I , $^{133\text{m}}\text{Te}$) that can
539 be compared with existing data. We also provide the ^{235}U cumulative yield for ^{132}I (circled
540 in Figure 15), which was not reported so far in prior publications. For the others, the
541 cumulative yields obtained in this work are consistent with existing data. In particular, we
542 observe a better agreement with Carrel *et al.* [7] than in our previous work. The prior
543 discrepancy was probably due to the poor knowledge of the geometry of the low-mass
544 HEU sample used in the previous experimental campaign [19]. The HEU sample used in
545 this work has a simpler geometry, i.e., a single fissile core instead of several cores separated
546 by Zircaloy spacers.

547 **6. Differentiation of actinide isotopes**

548 As photofission cross sections are of the same order of magnitude for all actinides, the
549 measured delayed gamma-ray signal can provide an estimation of the total nuclear material
550 mass. However, it does not indicate whether it is uranium or plutonium (with very different
551 specific activities, in Bq/g, which is essential for waste management especially for the long-
552 term alpha activity [34]), fissile or fertile isotopes (for criticality safety purpose in waste
553 package transport, interim storage, or final repository). This section deals with the
554 possibility to differentiate actinides using delayed gamma-ray ratios of their photofission
555 products.

556 When photofission occurs, the formation of two asymmetric fission fragments is the
557 most likely to happen, resulting in a mass distribution curve of the fission products
558 comporting two bumps: one for a heavy nucleus centered around mass number 140, and
559 one for a light nucleus centered around 95. Examples of this theoretical mass distribution
560 for photofission products are given in the work of Bernard *et al.* [22] and reported in Figure
561 16 for several actinides.

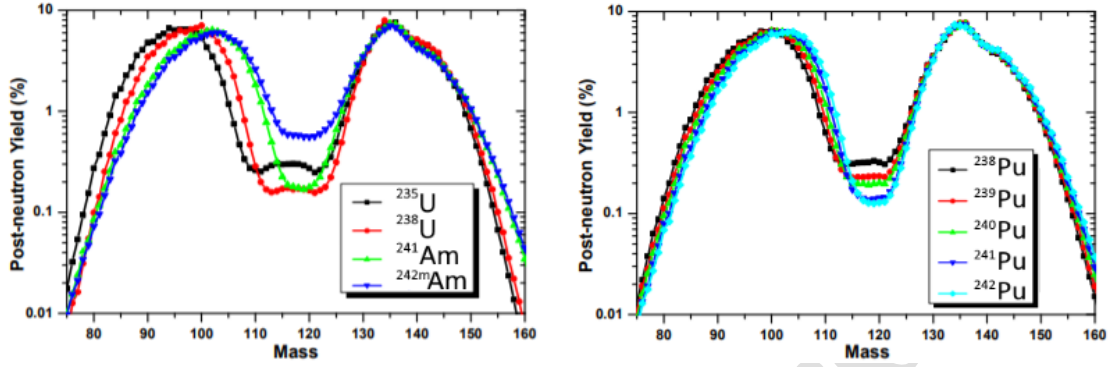


Figure 16: Independent photofission mass yields obtained with the GEF code [35], as reported in ref. [22].

562

563

564

565

566

567

568

569

570

571

572

573

574

575

576

577

578

A differentiation information can be obtained between uranium or plutonium isotopes thanks to their different photofission product yields, through the measurement of the relative intensities of specific delayed gamma lines emitted by photofission products having different yields for the different actinides [1][17]. The enrichment, defined as the proportion of the actinide(s) of interest in the mixture, can thus be computed from the ratio of two net areas and from the ratios of the photofission yields of their two emitting photofission products. The objective is to select specific photofission products pairs showing the largest differences, according to the actinide, in their gamma ratios. Some important parameters such as the energy of the gamma rays emitted by the photofission products (related to possible interferences with gamma rays of activation products, matrix attenuation effects, and the level of the Compton continuum under the peaks) and their intensity that determines the achievable counting statistics will also need to be taken into account to identify the most efficient photofission product couples.

For a mixture of ^{235}U and ^{238}U , the net peak area of a delayed gamma-ray line of energy

E_i emitted by photofission product j is given by (5):

$$A_j(E_i) = \frac{I(E_i)\varepsilon(E_i)N_A}{\lambda_j} \times (1 - e^{-\lambda_j t_{irr}}) \times e^{-\lambda_j t_{cool}} \times (1 - e^{-\lambda_j t_{count}}) \times \dots \left[Y_{j5} \frac{\alpha m_u}{\mathcal{M}_5} \int_{E_{threshold}}^{E_{max}} \varphi(E) \sigma_5(E) dE + Y_{j8} \frac{(1 - \alpha) m_u}{\mathcal{M}_8} \int_{E_{threshold}}^{E_{max}} \varphi(E) \sigma_8(E) dE \right] \quad (5)$$

579

Where:

580

- $A_j(E_i)$ is the net peak area of the gamma-ray line of energy E_i emitted by photofission product j ;

581

582

- $I(E_i)$ is the gamma-ray emission intensity;

- 583 - $\varepsilon(E_i)$ is the detection efficiency at energy E_i ;
- 584 - N_A is the Avogadro constant (in mol^{-1});
- 585 - λ_j is the radioactive decay constant of photofission product j (in s^{-1});
- 586 - t_{irr} , t_{cool} and t_{count} are respectively the irradiation, cooling and counting times
- 587 (in s);
- 588 - Y_{j5} and Y_{j8} are the cumulative yields of photofission product j for ^{235}U and ^{238}U ,
- 589 respectively;
- 590 - m_u is the total uranium mass (in g);
- 591 - \mathcal{M}_5 and \mathcal{M}_8 are respectively the molar masses of ^{235}U and ^{238}U (in $\text{g}\cdot\text{mol}^{-1}$);
- 592 - α is the enrichment, i.e. the proportion of ^{235}U in the uranium mixture;
- 593 - $E_{threshold}$ is the threshold energy of the photofission reaction;
- 594 - E_{max} is the endpoint energy of the Bremsstrahlung photon beam;
- 595 - $\varphi(E)$ is the Bremsstrahlung photon flux at energy E (in $\text{cm}^{-2}\cdot\text{s}^{-1}$);
- 596 - $\sigma_5(E)$ and $\sigma_8(E)$ are the photofission cross sections (in cm^2) at energy E for ^{235}U
- 597 and ^{238}U , respectively.

598

599 (5) can be rearranged and written as (6):

$$A_j(E_i) = k_j(E_i) \times m_u \times [Y_{j8}(\alpha - 1) - \Sigma \alpha Y_{j5}] \quad (6)$$

600 With:

- 601 - $k_j(E_i)$ a constant defined for the sake of simplification, which depends on the
- 602 photofission product radioactive constant, the gamma-ray intensity and detection
- 603 efficiency, and the measurement time parameters (irradiation, cooling, counting):

$$604 \quad k_j(E_i) = \frac{I(E_i)\varepsilon(E_i)N_A}{\lambda_j} \times (1 - e^{-\lambda_j t_{irr}}) \times e^{-\lambda_j t_{cool}} \times (1 - e^{-\lambda_j t_{count}}) \text{ (in } \text{s}^{-1}\cdot\text{mol}^{-1}\text{);}$$

- 605 - Σ another simplification constant depending on the actinide mixture, defined as:

$$606 \quad \Sigma = \frac{\frac{1}{\mathcal{M}_5} \int_{E_{threshold}}^{E_{max}} \varphi(E) \sigma_5(E) dE}{\frac{1}{\mathcal{M}_8} \int_{E_{threshold}}^{E_{max}} \varphi(E) \sigma_8(E) dE} \approx \frac{\int_{E_{threshold}}^{E_{max}} \varphi(E) \sigma_5(E) dE}{\int_{E_{threshold}}^{E_{max}} \varphi(E) \sigma_8(E) dE}.$$

607

608 Then, the ratio of the net areas of two delayed gamma rays emitted by two different

609 photofission products is given by (7):

$$R = \frac{k_1}{k_2} \times \frac{Y_{18}(\alpha - 1) - \Sigma\alpha Y_{15}}{Y_{28}(\alpha - 1) - \Sigma\alpha Y_{25}} = \frac{k_1}{k_2} \times R' \quad (7)$$

610 Where:

- 611 - k_1 and k_2 correspond to constants $k_j(E_i)$ described in (6). It is important to
- 612 mention that we are not limited to ratios of close-in-energy gamma rays. This
- 613 implies that detection efficiency at both energies has to be estimated and requires
- 614 a prior localization of actinides, for example with the method described in [18];
- 615 - α and Σ have the same meaning as in (5) and (6);
- 616 - Y_{18} and Y_{15} are the cumulative yields for the first photofission product for ^{238}U and
- 617 ^{235}U , respectively;
- 618 - Y_{28} and Y_{25} are the cumulative yields for the second photofission product for ^{238}U
- 619 and ^{235}U , respectively;
- 620 - R' is the net area ratio R corrected by the ratio of constants k_1 and k_2 taking into
- 621 account gamma-ray intensities and detection efficiencies of the two photofission
- 622 product gamma rays, and irradiation parameters of the two photofission products
- 623 (exponential terms in (5)).

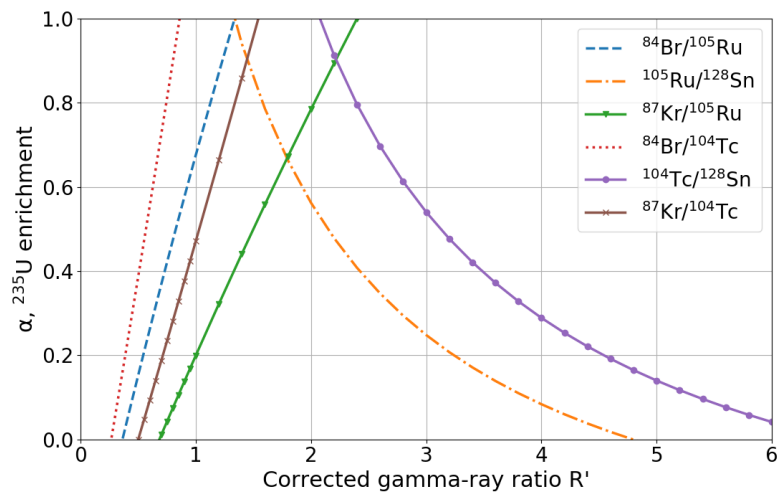
624

625 The efficiency of this differentiation method can be assessed by defining a criterion δ
 626 based on the variability of the calculated enrichment compared to the variability of the
 627 corrected gamma-ray ratio (8).

$$\delta = \frac{d\alpha}{dR'} \frac{R'}{\alpha} = \frac{\Sigma(Y_{15}Y_{28} - Y_{25}Y_{18})}{\left[\left(\frac{Y_{18}(\alpha - 1) - \Sigma\alpha Y_{15}}{Y_{28}(\alpha - 1) - \Sigma\alpha Y_{25}} \right) (Y_{28} - \Sigma Y_{25}) - Y_{18} + \Sigma Y_{15} \right]^2} \cdot \frac{Y_{18} \frac{\alpha - 1}{\alpha} - \Sigma Y_{15}}{Y_{28}(\alpha - 1) - \Sigma\alpha Y_{25}} \quad (8)$$

628 By minimizing this criterion over the whole enrichment range, the most appropriate
 629 photofission product couples can be identified based on their cumulative photofission
 630 product yields reported in previous section for ^{235}U and ^{238}U . The six most efficient
 631 photofission product couples for ^{235}U vs. ^{238}U discrimination are thus $^{84}\text{Br}/^{105}\text{Ru}$,
 632 $^{105}\text{Ru}/^{128}\text{Sn}$, $^{87}\text{Kr}/^{105}\text{Ru}$, $^{84}\text{Br}/^{104}\text{Tc}$, $^{104}\text{Tc}/^{128}\text{Sn}$ and $^{87}\text{Kr}/^{104}\text{Tc}$. The curves representing the
 633 ^{235}U enrichment as a function of the R' corrected ratio (deduced from the R measured ratio)
 634 are provided in Figure 17, showing that it seems possible to estimate α (or at least the

635 enrichment range) with the different couples if R' is measured with a reasonably low
 636 uncertainty, which will mainly depend on counting statistics uncertainties of the delayed
 637 gamma-ray net areas. For instance, a 20 % uncertainty on R' will convert to a relative
 638 uncertainty of 65 % on the ^{235}U enrichment, α , for the couple $^{87}\text{Kr}/^{105}\text{Ru}$ and a limited
 639 enrichment ($\alpha=0.2$). Besides, a 20 % uncertainty on R' for the couple $^{84}\text{Br}/^{105}\text{Ru}$
 640 corresponds to a relative uncertainty of 30 % on α for a higher enrichment ($\alpha=0.6$). A
 641 combination of the results, such as a weighted average of the enrichments obtained with
 642 the different couples, will probably be valuable. Further investigation will be conducted to
 643 demonstrate the differentiation efficiency of these photofission product couples on real
 644 actinide mixtures placed inside a matrix.



645

646 *Figure 17: Evolution of ^{235}U enrichment as a function of R' corrected ratio for the 6 most efficient photofission product*
 647 *couples in a $^{235}\text{U}/^{238}\text{U}$ mixture.*

648 Beyond a simple uranium mixture only, the photofission product yield values show that a
 649 differentiation of the fertile isotope (^{238}U) and the fissile ones (^{235}U and ^{239}Pu considered
 650 as a whole), could be achieved since the photofission cross-sections of ^{235}U and ^{239}Pu are
 651 similar and that of ^{238}U is way different, as shown in Figure 18. Indeed, there is only a 21%
 652 difference between the photofission rate in ^{239}Pu and ^{235}U for the 17.5 MeV endpoint
 653 energy Bremsstrahlung spectrum presented in this paper.

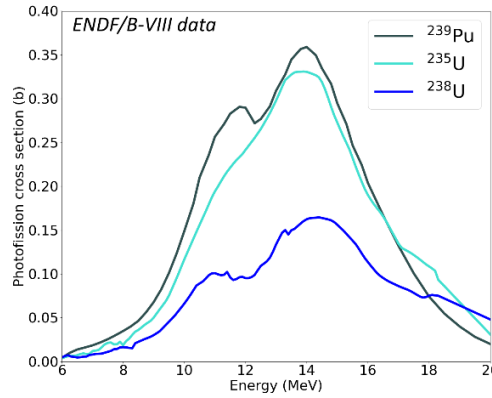


Figure 18: Photofission cross sections of ^{235}U , ^{238}U and ^{239}Pu [23].

654

655

656 The most efficient photofission product couple for that purpose is $^{128}\text{Sn}/^{134}\text{Te}$. The two

657 isotopes share a similar ratio of cumulative yields for ^{235}U $\left(\frac{Y_c(^{128}\text{Sn})}{Y_c(^{134}\text{Te})} = 0.23 \pm 0.06\right)$ and

658 ^{239}Pu $\left(\frac{Y_c(^{128}\text{Sn})}{Y_c(^{134}\text{Te})} = 0.23 \pm 0.05\right)$, and a different ratio for ^{238}U $\left(\frac{Y_c(^{128}\text{Sn})}{Y_c(^{134}\text{Te})} = 0.10 \pm 0.02\right)$.

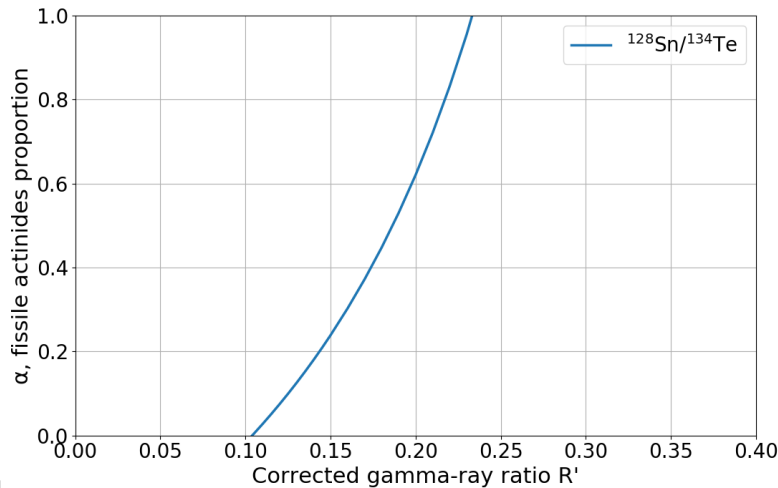
659 Therefore, ^{235}U and ^{239}Pu can be regarded as a global fissile mass that can be differentiated

660 from ^{238}U mass. The curve representing the fissile actinides proportion as a function of the

661 R' corrected ratio (deduced from the R measured ratio) is provided in Figure 19. Note that

662 the contrast for the differentiation between $^{235}\text{U}+^{239}\text{Pu}$ and ^{238}U is lower compared to the

663 differentiation between ^{235}U and ^{238}U in Figure 17.



664

665

666

Figure 19: Evolution of the fissile actinides proportion in a $^{235}\text{U}/^{239}\text{Pu}/^{238}\text{U}$ mixture as a function of R' corrected ratio for the couple $^{128}\text{Sn}/^{134}\text{Te}$

667 It is worth noting that such a global fissile vs. fertile actinides differentiation based on

668 photofission had not been proposed yet, as the yields of these fission products reported in

669 the literature are scarce for ^{235}U or ^{239}Pu , for instance only one measured yield was reported
670 so far concerning ^{128}Sn and ^{134}Te photofission products of ^{239}Pu .

671 7. Conclusion

672 New measurements of cumulative photofission yields with a 17.5 MeV endpoint
673 Bremsstrahlung photon beam produced by a SATURNE electron LINAC have been
674 performed in CINPHONIE facility, at CEA Cadarache IRESNE Institute, France. To this
675 aim, a characterization of the Bremsstrahlung photon beam has been first carried out by
676 photon activation analysis with different samples of Au, Ni, U, Zn and Zr. In a former
677 study, we highlighted that most of neutron fissions arise from fast neutrons produced in the
678 actinide sample itself, but not from the photoneutron production in the LINAC components
679 (target, collimator). As a result, the neutron fission rate in the different samples has been
680 numerically estimated with MCNP to subtract it from the total fission rate. Finally, the
681 cumulative production yields of 26 photofission products have been measured for ^{239}Pu
682 and ^{235}U and 28 have been evaluated for ^{238}U . Four of them are not reported in the literature
683 for ^{239}Pu , and one for ^{235}U . Among these available photofission product yields, some show
684 large discrepancies between actinides and thus appear as good candidates for their
685 differentiation based on gamma-ray ratios. To that extent, the six most efficient couples
686 enabling the differentiation between ^{235}U and ^{238}U have been determined. Furthermore, a
687 photofission products couple ($^{128}\text{Sn}/^{134}\text{Te}$) has been identified for the differentiation
688 between fissile ($^{235}\text{U}+^{239}\text{Pu}$) and fertile (^{238}U) isotopes in a mixture of uranium and
689 plutonium.

690 Further work will be dedicated to the selection of the most efficient photofission product
691 couples in presence of a waste matrix, causing gamma attenuation effects that depend on
692 actinide localization. To this aim, a new experimental campaign will be carried out to test
693 the differentiation of actinide isotopes inside a concrete matrix, as reported in [18] for
694 actinide localization. One of the main objectives of this long-term R&D program is to
695 assess nuclear materials in heterogeneous technological waste blocked in 870 L cemented
696 drums. Therefore, the quantification of their mass and the differentiation of actinides will
697 be finally tested with an 870 L mock-up drum with uranium and plutonium samples inside.

698 **Acknowledgements**

699 The authors would like to thank the French National Radioactive Waste Management
700 Agency (ANDRA) contributing for several years to this research and development activity
701 within a cooperation framework under the COV – F32678 DEN4908 – C43R9T5480
702 contract.

703 **References**

- 704 [1] F. Carrel, M. Agelou, M. Gmar, F. Lainé, J. Loridon, J.-L. Ma, C. Passard, B.
705 Poumarède, “*Identification and Differentiation of Actinides Inside Nuclear Waste*
706 *Packages by Measurement of Delayed Gammas*”, IEEE Trans. Nucl. Sci., 57 (5)
707 2862, (2010).
- 708 [2] F. Carrel, M. Agelou, M. Gmar, F. Lainé, “*Detection of high-energy delayed*
709 *gammas for nuclear waste packages characterization*”, Nuclear Instruments and
710 Methods in Physics Research Section A, vol. 652 (1), 137-139 (2011).
- 711
- 712 [3] T. Nicol, B. Pérot, C. Carasco, F. Brackx, A. Mariani, C. Passard, E. Mauerhofer, J.
713 Collot, “*Feasibility study of ^{235}U and ^{239}Pu characterization in radioactive waste*
714 *drums using neutron-induced fission delayed gamma rays*”, Nuclear Instruments
715 and Methods in Physics Research Section A, vol. 832, 85-94 (2016).
- 716
- 717 [4] R. De Stefano, C. Carasco, B. Pérot, E. Simon, T. Nicol, E. Mauerhofer, “*Feasibility*
718 *study of fissile mass detection in 870 L radioactive waste drums using delayed*
719 *gamma rays from neutron-induced fission*”, Journ. Radioanal. Nucl. Chem., vol.
720 322, 1185-1194 (2019).
- 721
- 722 [5] E. Simon, F. Jallu, B. Pérot, S. Plumeri, “*Feasibility study of fissile mass*
723 *quantification by photofission delayed gamma rays in radioactive waste packages*
724 *using MCNPX*”, Nuclear Instruments and Methods in Physics Research Section A,
725 vol. 840, 28-35, (2016).

726

727 [6] S. Kahane, A. Wolf, “*Photofission of ^{238}U with neutron-capture gamma rays*”,
728 Phys. Rev. C, vol. 32, no 6, (1985).

729

730 [7] F. Carrel, M. Agelou, M. Gmar, F. Lainé, J. Lorida, J.-L. Ma, C. Passard, (...), B.
731 Poumarède, “*New Experimental Results on the Cumulative Yields From Thermal*
732 *Fission of ^{235}U and ^{239}Pu and From Photofission of ^{235}U and ^{238}U Induced by*
733 *Bremsstrahlung*”, IEEE Transactions on Nuclear Science, 58, 2064-2072, (2011).

734

735 [8] H. Naik, V. T. Nimje, D. Raj, S. V. Suryanarayana, A. Goswami, S. Singh, S. N.
736 Acharya, K. C. Mittal, S. Ganesan, P. Chandrachoodan, V. K. Manchanda, V.
737 Venugopal, S. Banarjee, “*Mass distribution in the bremsstrahlung-induced fission*
738 *of ^{232}Th , ^{238}U and ^{240}Pu ”, Nucl. Phys. A 853, 1 (2011).*

739

740 [9] H. Naik, F. Carrel, G. N. Kim, F. Laine, A. Sari, S. Normand, A. Goswami, “*Mass*
741 *yield distributions of fission products from photo-fission of ^{238}U induced by 11.5-*
742 *17.3 MeV bremsstrahlung*”, Eur. Phys. J. A 49, 94 (2013).

743

744 [10] H. Naik, B. S. Shivashankar, H. G. Raj Prakash, D. Raj, G. Sanjeev, N. Karunakara,
745 H. M. Somashekarappa, S. Ganesan, G. N. Kim, A. Goswami, “*Measurements of*
746 *fission yield in 8 MeV bremsstrahlung induced fission of ^{232}Th and ^{238}U ”, J.*
747 *Radioanal. Nucl. Chem.* 299, 127 (2014).

748

749 [11] X. Wen, H. Yang, “*Photofission product yields of ^{238}U and ^{239}Pu with 22-MeV*
750 *bremsstrahlung*”, Nuclear Instruments and Methods in Physics Research Section A,
751 vol. 821, 34 (2016).

752

753 [12] Krishichayan, Megha Bhike, C. R. Howell, A. P. Tonchev, W. Tornow, “*Fission*
754 *product yields measurements using monoenergetic photon beams*”, Physical
755 Review C 100, 014608 (2019).

756

- 757 [13] M. Ya. Kondrat'ko, A. V. Mosesov, K. A. Petrzhak, O. A. Teodorovich, "Yields of
758 *photofission of ^{239}Pu* ", *Atomnaya Energiya*, vol. 50, no 1, 34-36 (1981).
- 759
760 [14] M. Bhike, W. Tornow, Krishichayan, A. P. Tonchev, "Exploratory study of fission
761 *product yield determination from photofission of ^{239}Pu at 11 MeV with*
762 *monoenergetic photons*", *Physical Review C* 95 (2017).
- 763
764 [15] C. L. Hollas, D. A. Close, C. E. Moss, "Analysis of fissionable material using
765 *delayed gamma rays from photofission*", *Nuclear Instruments and Methods in*
766 *Physics Research Section B*, vol. 24-25, Part 1, 503-505 (1987).
- 767
768 [16] D. H. Beddingfield, F. E. Cecil, "Identification of fissile materials from fission
769 *product gamma-ray spectra*", *Nuclear Instruments and Methods in Physics*
770 *Research Section A*, vol. 417, 405-412 (1998).
- 771
772 [17] M. Gmar, J.M. Capdevila, "Use of delayed gamma spectra for detection of
773 *actinides (U,Pu) by photofission*", *Nuclear Instruments and Methods in Physics*
774 *Research Section A*, vol. 422, 841-845 (1999).
- 775
776 [18] M. Delarue, Eric Simon, Bertrand Pérot, Pierre-Guy Allinei, Nicolas Estre, Daniel
777 Eck, Emmanuel Payan, David Tisseur, O. Gueton, Denise Ricard and Johann Collot,
778 "Localization of nuclear materials in large concrete radioactive waste packages
779 using photofission delayed gamma rays" *EPJ Web of Conferences* 253, 08003
780 (2021)
- 781
782 [19] M. Delarue, E. Simon, B. Pérot, P.G. Allinei, N. Estre, E. Payan, D. Eck, D.
783 Tisseur, I. Espagnon, J. Collot, "Measurement of cumulative photofission yields of
784 ^{235}U and ^{238}U with a 16 MeV Bremsstrahlung photon beam", *Nuclear Instruments*
785 *and Methods in Physics Research Section A*, vol. 1011 (2021).
- 786
787 [20] B. Pérot, F. Jallu, C. Passard, O. Gueton, P.-G. Allinei, L. Loubet, N. Estre, E.
788 Simon, C. Carasco, C. Roure, L. Boucher, H. Lamotte, J. Comte, M. Bertaux, A.
789 Lyoussi, P. Fichet, F. Carrel, "The characterization of radioactive waste: a critical

- 790 *review of techniques implemented or under development at CEA, France*”, EPJ
791 Nuclear Sciences and Technologies 4, 3 (2018).
- 792
793 [21] M. Bricka, V.-D. Nguyen, L. Porthéos, “*Le spectromètre neutrons à activation*
794 *SNAC – Principe – Description – Utilisation*”, CEA R-4226 report (1971).
- 795
796 [22] D. Bernard, O. Sérot, E. Simon, L. Boucher and S. Plumeri, “*A Photofission*
797 *Delayed γ -ray Spectra Calculation Tool for the Conception of a Nuclear Material*
798 *Characterization Facility*”, EPJ Web of Conferences 170, 06001 (2018).
- 799
800 [23] D.A. Brown, *et al.*, “*ENDF/B-VIII.0: The 8th Major Release of the Nuclear*
801 *Reaction Data Library with CIELO-project Cross Sections, New Standards and*
802 *Thermal Scattering Data*”, Nucl. Data Sheets 148, 1-142 (2018).
- 803
804 [24] A-C. Simon, J-P. Both, I. Espagnon, J. Lefevre, V. Picaud, A. Pluquet, “*A new*
805 *computer code for the determination of the isotopic composition of actinides by X-*
806 *and gamma-ray spectrometry and its applications*”, European Nuclear Conference
807 2005, France (2006).
- 808
809 [25] A-C. Simon, F. Carrel, I. Espagnon, M. Lemerancier and A. Pluquet, “*Determination*
810 *of Actinide Isotopic Composition: Performances of the IGA Code on Plutonium*
811 *Spectra according to the Experimental Setup*”, IEEE Transactions on Nuclear
812 Science, vol 58, no 2 (2011).
- 813
814 [26] A. J. M. Plompen, O. Cabellos, C. De Saint Jean *et al.* The joint evaluated fission
815 and fusion nuclear data library, JEFF-3.3. Eur. Phys. J. A 56 181 (2020).
- 816
817 [27] R. Nath, R.-J. Schulz, “*Determination of high-energy X-ray spectra by*
818 *photoactivation*”, Medical Physics, vol. 3, no. 3, 133-141 (1975).
- 819
820 [28] Los Alamos National Laboratory, *Mcnp 6TM User’s Manual*, Denise B. Pelowitz
821 (2013).
- 822

- 823 [29] N. Otuka, E. Dupont, V. Semkova, B. Pritychenko, A. I. Blokhin, M. Aikawa, S.
824 Babykina, M. Bossant, G. Chen, S. Dunaeva, R. A. Forrest, T. Fukahori, N.
825 Furutachi, S. Ganesan, Z. Ge, O. O. Gritzay, M. Herman, S. Hlavač, K. Katō, B.
826 Lalremruata, Y. O. Lee, A. Makinaga, K. Matsumoto, M. Mikhaylyukova, G.
827 Pikulina, V. G. Pronyaev, A. Saxena, O. Schwerer, S. P. Simakov, N. Soppera, R.
828 Suzuki, S. Takács, X. Tao, S. Taova, F. Tárkányi, V. V. Varlamov, J. Wang, S. C.
829 Yang, V. Zerkin, Y. Zhuang, *"Towards a More Complete and Accurate*
830 *Experimental Nuclear Reaction Data Library (EXFOR): International*
831 *Collaboration Between Nuclear Reaction Data Centres (NRDC)"*, Nucl. Data
832 Sheets 120, 272-276 (2014).
- 833
- 834 [30] C. Plaisir *et al.*, *"Measurement of the $^{85}\text{Rb}(\gamma, n)^{84\text{m}}\text{Rb}$ cross-section in the energy*
835 *range 10–19 MeV with bremsstrahlung photons"*, Eur. Phys. Journal A 48:68
836 (2012). (EXFOR G0033.002).
- 837
- 838
- 839 [31] H. Bateman, *"The solution of a system of differential equations occurring in the*
840 *theory of radioactive transformations"*, Proc. Cambridge Philosophical Society,
841 vol. 15, 423-427 (1910).
- 842
- 843 [32] P. Leconte, J. P. Hudelot and M. Antony, *"Accurate γ -ray spectrometry*
844 *measurements of the half-life of ^{92}Sr "*, Applied Radiation and Isotopes, vol. 66, issue
845 10, 1450-1458 (2008).
- 846
- 847 [33] O. O. Parlag, V. T. Maslyuk, E. V. Oleynikov, I. V. Pylypchynets, A. I. Lengyel,
848 *"Product yields for the photofission of ^{239}Pu with bremsstrahlung at 17.5 MeV*
849 *boundary energy"*, Problems of Atomic Science and Technology, vol. 136 (2021).
- 850
- 851 [34] ANDRA (French Radioactive Waste Management Agency), Radioactive waste
852 classification, website: [https://international.andra.fr/radioactive-waste-](https://international.andra.fr/radioactive-waste-france/waste-classification)
853 [france/waste-classification](https://international.andra.fr/radioactive-waste-france/waste-classification).

854

- 855 [35] K.-H. Schmidt, B. Jurado, C. Amouroux, C. Schmitt, “*General Description of*
856 *Fission Observables: GEF model code*”, Nucl. Data Sheets, vol. 131, 107-221
857 (2016).

Journal Pre-proof

Highlights

- Photofission is a promising technique to assay nuclear waste packages
- Photon activation analysis is used to characterize a 17.5 MeV Bremsstrahlung beam
- Photofission products cumulative yields have been determined for ^{239}Pu , ^{235}U and ^{238}U
- The contribution of neutron fission has been estimated with the MCNP code
- Photofission product yield difference makes actinides differentiation practicable

Journal Pre-proof

CRedit author statement:

M. Delarue: Methodology, Investigation, Software, Writing – Original Draft, Visualization, Formal analysis

E. Simon: Conceptualization, Methodology, Writing – Review & Editing

B. Pérot: Supervision, Writing – Review & Editing

P.G. Allinei: Software, Investigation, Resources

N. Estre: Investigation, Resources

E. Payan: Investigation, Resources

D. Eck: Investigation, Resources

I. Espagnon: Software

J. Collot: Supervision, Writing – Review & Editing

Journal Pre-proof

Declaration of interests

The authors declare that they have no known competing financial interests or personal relationships that could have appeared to influence the work reported in this paper.

The authors declare the following financial interests/personal relationships which may be considered as potential competing interests:

Journal Pre-proof